Healthcare and Rehabilitation Robotics
German Aerospace Center (DLR)
TUM School of Engineering and Design

TECHNICAL UNIVERSITY OF MUNICH

Master's Thesis in Medical Technology and Assistance Systems

Design and Validation of a Customizable Electromyographic Sensor Module for the DLR Research Wristband

Hans Große-Westermann

Healthcare and Rehabilitation Robotics
Deutsches Zentrum für Luft- und Raumfahrt (DLR)
TUM School of Engineering and Design

TECHNICAL UNIVERSITY OF MUNICH

Master's Thesis in Medical Technology and Assistance Systems

Design and Validation of a Customizable Electromyographic Sensor Module for the DLR Research Wristband

Author:	Hans Große-Westermann
Examiner:	Prof. Dr. Cristina Piazza
Supervisor:	Konrad Fründ
Submission Date:	31.08.2025

I confirm that this master's thesis is my own work and I have documented all sources and material used.

Munich, 31.08.2025 Hans Große-Westermann

Acknowledgments

I used Perplexity AI as a tool to help rephrase and improve clarity of the written content. All outputs were reviewed and edited.

Abstract

This master's thesis presents the design and validation of a customizable surface electromyography sensor module tailored for integration into the DLR research wristband, a modular wearable platform aimed at advancing human-machine interfaces. Surface electromyography enables the non-invasive detection of electrical activity produced by skeletal muscles, providing valuable insights into user intent for controlling assistive devices and interactive systems. The thesis addresses critical challenges in sEMG signal acquisition, such as minimizing power line interference, optimizing signal-to-noise ratio, and improving spatial and temporal resolution through electrode and circuit design.

A systematic approach was employed involving circuit simulation, circuit and electrode design, and sensor module validation. Four circuit topologies, single differential with three or six electrodes, double differential with four electrodes, and monopolar with six electrodes, were designed and analyzed. Simulations evaluate gain, common-mode rejection ratio, and frequency response. Sensor modules were validated in comparison to a commercial sEMG system. Experiments employed an isometric contraction protocol on the biceps brachii across multiple load levels to assess signal quality, frequency characteristics, and the ability to detect propagating motor unit action potentials.

Results demonstrated that the designed sensor modules achieved comparable signal-to-noise ratios to the commercial reference system, although steel electrodes presented challenges related to increased common-mode noise that could be mitigated by notch filtering. The results revealed that single and double differential acquisition modes significantly affect the amplitude and frequency characteristics of measured EMG signals, which must be considered when interpreting sEMG data or designing sensor systems. The integration of the sensor module into the DLR research wristband was successfully validated through a multi-subject study, confirming consistent sEMG acquisition under various loading conditions and highlighting battery-powered operation benefits.

The findings substantiate the feasibility of a customizable, modular sEMG solution for wearable applications.

Contents

1 Introduction

Human-Machine interfaces (HMI) play a crucial role in the modern society. From smartphones and computers to complex machinery, our ability to interact efficiently with electronic devices significantly impacts productivity, convenience and safety. One key aspect of HMI is intent detection, which is explored through various methods, including Surface Electromyography (sEMG).

EMG allows for the measurement of electrical activity produced by the skeletal muscles [1]. By processing this data, it is possible to estimate the user's movement intentions. The Myo armband, developed by Thalmic Labs in 2015, was one of the first devices to use EMG for gesture recognition [2] (Figure 1.1) A. The Myo armband enables a comparable database of machine learning algorithms with the same set of hardware, which was crucial to the fields success.

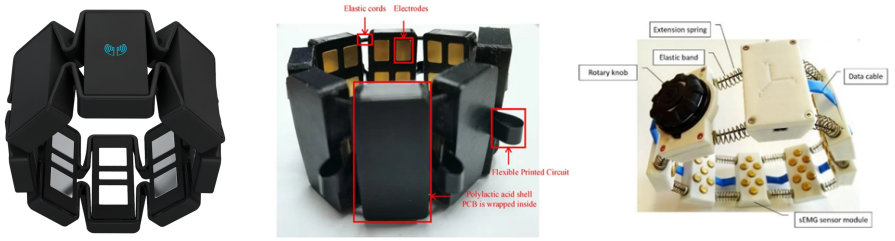

Figure 1.1: A: Myo Armband, Thalmic Labs [3], B: Research Wristband [4], C: Research Wristband [5]

Since the discontinuation of the Myo Armband in 2018, numerous research wristbands with different sensor modalities have been developed, indicating the potential of the field (Figure 1.1 B, C). The commercial interest of such a technology can be underscored by Metas sEMG-based HMI in their metaverse research [6]. However, neither Metas HMI nor any other comparable wristbands with sufficient resolution are commercially available.

The German Aerospace Senter (DLR) research wristband (Figure 1.2 A) was designed

to integrate different sensor modalities into one low-cost device [7]. This modular wristband can support up to 30-35 modules, providing high spatial resolution. It includes a data transmission protocol for interfacing sensor modules and the periphery (Figure 1.2, B).

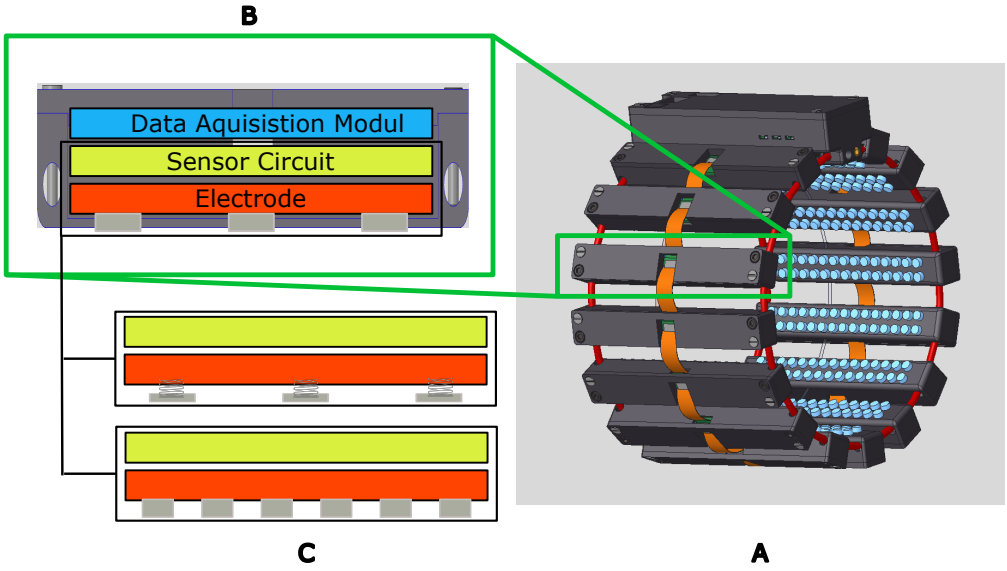

Figure 1.2: A: Rendering of theDLR Research Wristband, B: sEMG Wristband Module, C: sEMG sensor modules

2 Background

The background chapter provides essential foundational knowledge on the physiological and technical principles underpinning sEMG. It introduces the biophysical basis of muscle activity, describes the anatomical and electrophysiological characteristics of muscle activation, and outlines the main factors influencing sEMG signal acquisition. Understanding these concepts is crucial for interpreting sEMG measurements and designing effective sEMG sensors and systems. This chapter also discusses acquisition techniques, signal properties, electrode design issues, and circuitry considerations relevant to high-quality sEMG recordings.

2.1 Physiology of Muscle Bio-electric Signals

To understand the working principle of sEMG sensors, it is necessary to know the underlying physiological principles of muscle activation.

Action Potential

The fundamental unit of bio-electric muscle activity is the action potential. It arises from a rapid, transient exchange of ions across the neuronal cell membrane. When a stimulus exceeds a voltage threshold at a neuron, voltage-gated sodium channels open, allowing sodium ions to enter the cell and causing depolarization. Subsequently, potassium channels open, potassium ions exit the cell, and the membrane repolarizes to its initial potential of around $-70\,\mathrm{mV}$ [8]. The action potential is an all-or-nothing event, meaning its amplitude remains constant and does not vary with stimulus intensity [9].

Muscle Innervation

The innervation of the skeletal muscles is the key mechanism for intentional human movements. Skeletal muscles are organized in a hierarchical structure that enables efficient force generation and transmission. Figure 2.1 shows the architecture of skeletal muscles from a macroscopic to a microscopic level. A skeletal muscle is composed of bundles called fascicles, each surrounded by connective tissue. Zooming in, each fascicle contains numerous elongated muscle fibers. Within each muscle fiber, myofibrils

are arranged in parallel and consist of repeating sarcomeres. Sarcomeres build the fundamental contractile units responsible for muscle contraction.

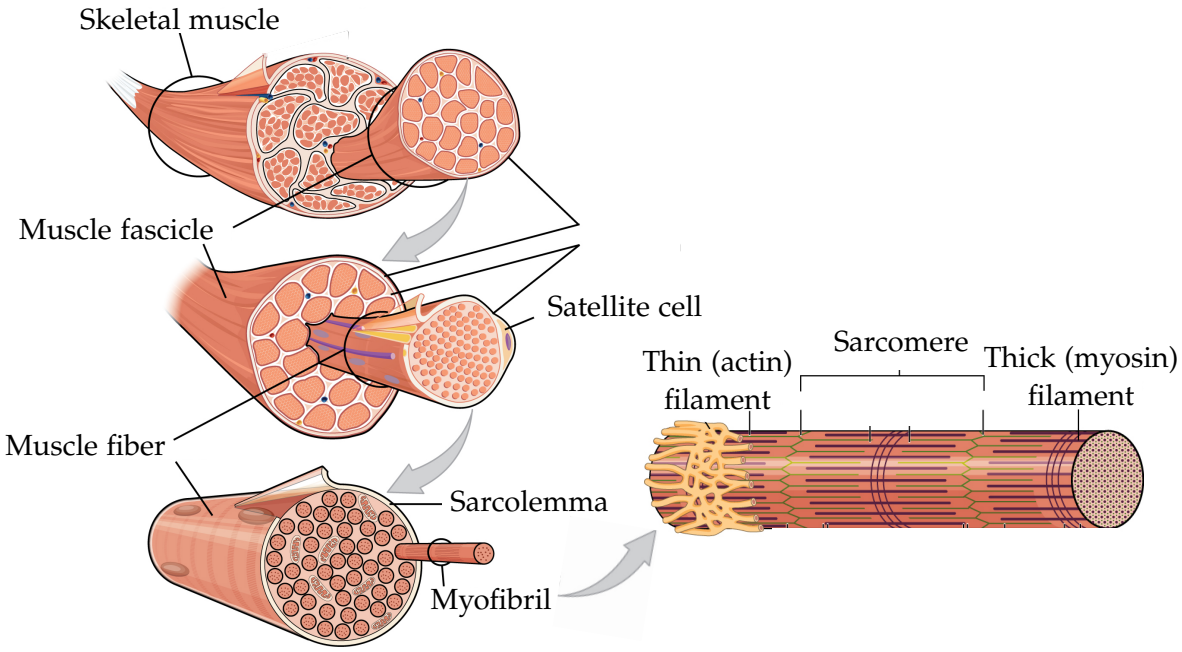

Figure 2.1: Skeletal muscle architecture adapted from [10]

During muscle contraction, the action potential is sent from neurons in the brain through the spinal cord along the axons of the motor neurons to the neuromuscular junction (Figure 2.2). One motor neuron innervates from 50 to over 1000 muscle fibers via neuromuscular junctions. Together, they form one motor unit (MU), first described in 1925 by Liddell and Sherrington [11]. All action potentials sent from one motor neuron to the muscle fibers of the motor unit is called motor unit action potential (MUAP). When a motor neuron fires, two action potentials propagate from the neuromuscular junction in opposite directions along the muscle fiber to the fiber-tendon junction. Neuromuscular junctions of one MU are spread over an area called the innervation zone. Over this zone, sEMG signal acquisition is not recommended due to the different propagation directions. The speed at which an action potential propagates along a muscle fiber, known as conduction velocity (CV), ranges between 4 to 5 m/s and is influenced by several factors such as fiber diameter, fiber length, and skin temperature [12, 13].

When a MUAP propagates through the muscle fiber it is causing the muscle fibers to contract. The amount of force a motor unit can generate depends primarily on

the number of innervated muscle fibers (innervation number) and the discharge rate [14]. The force output of a muscle is regulated through two primary mechanisms: Recruitment of additional motor units and an increase in discharge rate of already active motor units [15]. The discharge rate describes the frequency at which a motor neuron "fires" and sends action potentials to the muscle fibers. Discharge rate and innervation number differ between types of muscles and the contraction levels [16]. Recruitment and temporal summation via increased discharge rates enables graded force production despite the invariant nature of individual action potentials.

Skeletal muscle fibers can be classified into three main types: slow-twitch (Type 1), fast-twitch oxidative (Type 2a), and fast-twitch glycolytic (Type 2x or 2b). Slow-twitch fibers contract slowly, are highly resistant to fatigue, and are specialized for endurance activities. Fast-twitch oxidative fibers contract more rapidly and generate more force, while still offering moderate resistance to fatigue. Fast-twitch glycolytic fibers contract the fastest and produce the greatest force but they fatigue quickly and are used for short, explosive movements. According to Henneman's size principle, motor units are recruited in a fixed order based on size: Smaller motor units , which innervate slow-twitch muscle fibers, are activated first during low-force contractions. As the demanded force increases, larger units are progressively recruited. These larger units innervate more fast-twitching fibers. This hierarchical recruitment optimizes force gradation and energy efficiency [17].

SEMG provides valuable insights into the muscle activation characteristics, including information about muscles fiber types. For example, a frequency analysis of the signal can reflect the underlying composition of fast and slow twitching fibers within a muscle. Muscles with a higher proportion of fast-twitch fibers tend to show higher median frequencies and conduction velocities, while muscles with more slow-twitch fibers show lower values [18].

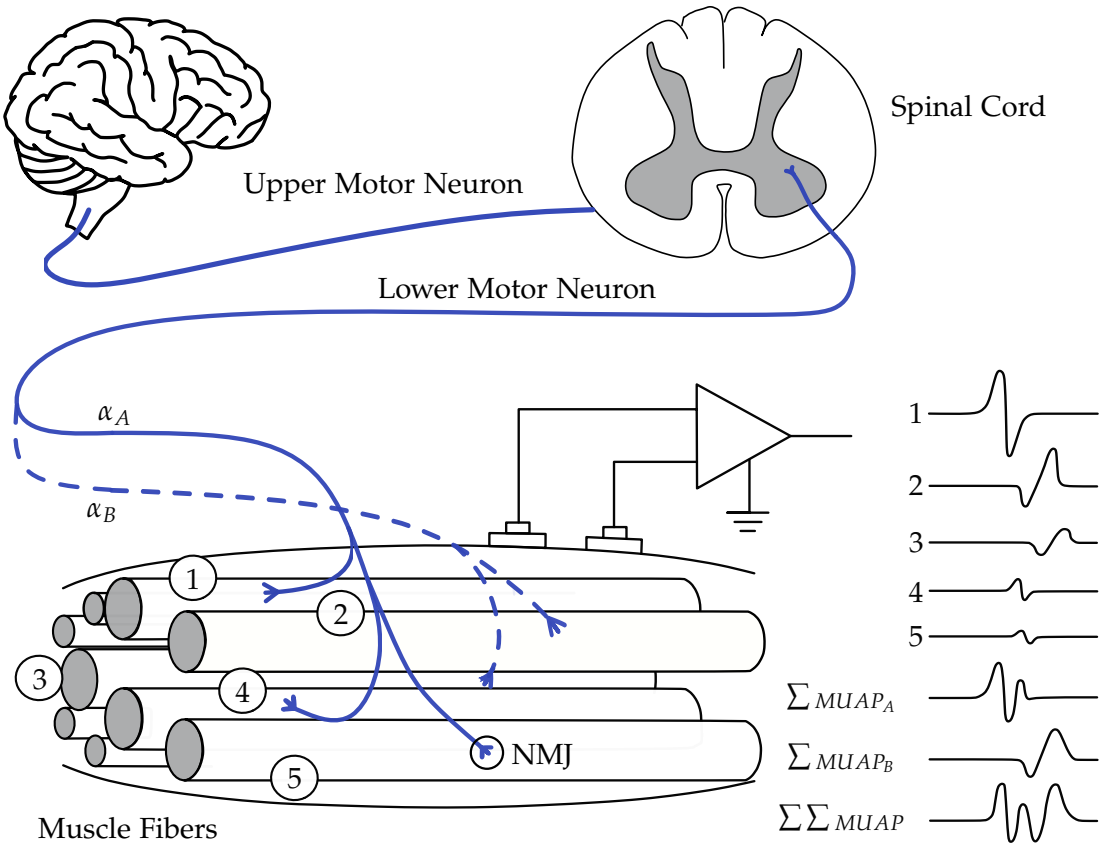

Figure 2.2: Simplified pathway of the and composition of an electromyogram. Adapted from [19]. 1, 2, 3, 4, 5: Muscle fibers, NMJ: Neuromuscular junction.

Figure 2.2 shows the simplified motor pathway over the brain stem and the spinal cord to the muscles fibers. Two MUs (A and B) are depicted. Muscles fiber 1, 4, and 5 are part of MU A, while muscle fibers 2 and 3 are being innervated by motor neuron B. The summation of the synchronized signals 1, 4, and 5 compose the MUAP of motor unit A. A sEMG sensor on the skin cannot detect individual MUAPs directly but the superimposed MUAPs ($\sum\sum_{MUAP}$). More superficial muscle fibers (1,2) contribute more strongly to the detected signal than muscles fibers further away from the skin. In order to detect individual MUAPs a multichannel sEMG is required.

SEMG Signal Characteristics

An understanding of the characteristics of the sEMG signals is required to perform suitable post-processing and interpretation of measurements. The waveform, amplitude

and spectral characteristics of the surface MUAP and the resulting sEMG signal are influenced by different geometrical and physiological factors, such as MU depth, electrode configuration, spread of the innervation zone, and muscle fiber type [20]. These features need to be considered when comparing measurements of different subjects. Average rectification, fast fourier transformation (FFT), and envelope functions are used to extract information out of the raw sEMG signal (Figure 2.3). The FFT converts the time-domain muscle electrical signals into the frequency domain, revealing the distribution of signal power across frequencies. The relevant frequencies of sEMG range from 5 to 500 Hz [21]. The frequency representation helps characterize muscle activation patterns, assess muscle fatigue, and differentiate physiological and pathological muscle conditions by identifying key spectral properties of the sEMG signal. It is important to note that, according to the Nyquist theorem, the sampling frequency must be at least twice the highest frequency contained in the muscle signal to avoid aliasing, which causes distortion and loss of information [22]. This means that for sEMG signals the sampling rate should be a minimum of 1000 Hz.

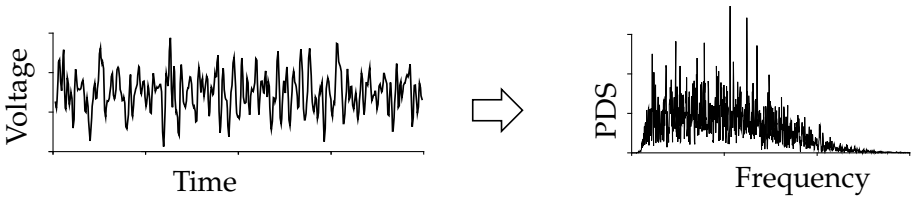

Figure 2.3: Typical Raw sEMG signal and its Power Density Spectrum

2.2 Electromyography Principles

A variety of fundamental principles affect the acquisition of sEMG signals. The characteristics of the recorded signal depend not only on the physiological processes of the muscle activation, but also on the design and configuration of the sensor system, the placement and properties of the electrodes, and the electrical environment in which the measurement takes place [14]. In addition to sEMG, intramuscular needle EMG represents an alternative approach where electrodes are inserted directly into muscle tissue to record MUAPs. However, surface sEMG is more suitable for wearable devices used in human-machine interface applications due to it non-invasive nature.

Several key factors play a role in determining the signal-to-noise ratio (SNR), precision, accuracy, and overall quality of sEMG recordings. These include the electrical interface between the skin and the electrode (which can introduce noise and voltage division effects), susceptibility to common-mode noise, crosstalk from adjacent muscles,

and geometric parameters such as electrodes size and inter-electrode distance (IED) [23], [24].

In the following subsections, the most relevant principles and their implications for sEMG sensor design and signal acquisition are discussed in detail.

2.2.1 Voltage Divider Effect

The electrode-skin interface together with input impedance of the amplifier form a critical voltage divider circuit that fundamentally impacts sEMG signal acquisition. This circuit attenuates the bio-electric signal and introduces noise, making its understanding essential for sEMG sensor design.

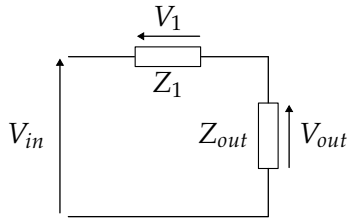

$$V_{out} = V_{in} \cdot \frac{Z_{out}}{Z_1 + Z_{out}}$$

Figure 2.4: Voltage Divider effect

The voltage divider effect describes how the output voltage is affected by an additional impedance that is in series with the impedance of the output (Figure 2.4). If $Z_{out} \gg Z_1$ the voltage that is "lost" at impedance Z_1 is insignificant.

2.2.2 Common Mode and Powerline Interference

Common-mode describes the electrical signals which are present at both inputs of a differential amplifier and do not represent the sEMG information of interest. Common-mode sources include ECG signals and end-of-fiber effects [25]. The end-of-fiber effect describes a spike of electrical potential when the propagating signal is extinguished at the muscle-tendon junction. Powerline interference (PLI) and common-mode noise are two of the main challenges in sEMG signal acquisition due to the low-amplitude of myoelectric signals. These artifacts arise primarily from capacitive coupling between the human body and the 50 Hz electromagnetic fields produced by the powerline interfering with the signal [26]. The body of a Person (P) is acting like an antenna by coupling with the power lines through parasitic capacitance (C_1,C_2) as shown in Figure 2.5.

This creates a common-mode voltage V_{cm} in the order of V and an AC current I_{AC} in the order of tens of nA [27]. For a differential measuring sEMG between electrodes e1

and electrode e2, the interference due to the common-mode is defined as follows:

$$V_{Noise} = V_{cm} \cdot \frac{Z_{e1} - Z_{e2}}{Z_i} \tag{2.1}$$

Z_{e1} and Z_{e2} represent the electrode-skin interface impedance and Z_i is the input impedance of the amplifier. An impedance imbalance ($Z_{e1} \neq Z_{e2}$) converts the common-mode noise to differential noise due to the voltage divider effect 2.1 [28].

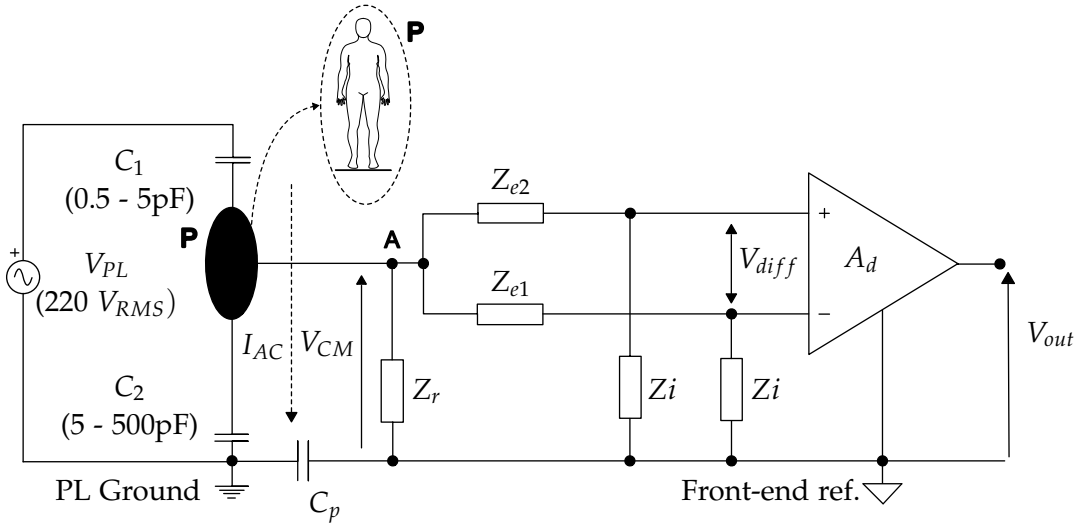

Figure 2.5: Equivalent circuit showcasing powerline interference. Adjusted from [27].

Figure 2.6 illustrates the effect of common-mode on sEMG characteristics. A large common-mode voltage can saturate the amplifiers, driving the sEMG signal beyond the permissible input range. In this state, portions of the signal are clipped, resulting in a loss of information.

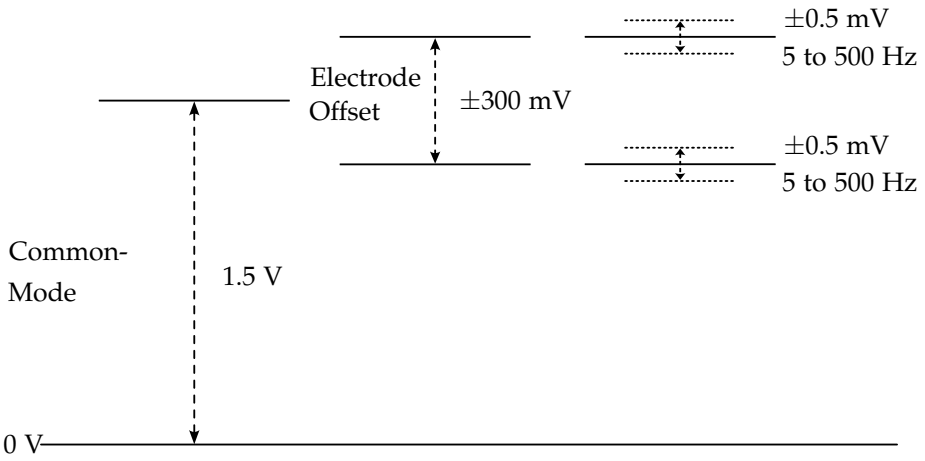

Figure 2.6: Composition of the sEMG signal influenced by common-mode and electrodes. Adapted from [29].

Attenuation of the sEMG signal is another direct consequence of the voltage divider effect of the electrode-skin impedance and the input of the differential amplifier Figure 2.4. This attenuation can be reduced by increasing the input impedance of the differential amplifier and reducing the electrode-skin impedance. PLI can also be mitigated by minimizing the imbalance between the impedance of electrode-skin interfaces. Contact impedance can vary from several kΩ to several MΩ, depending on the size an material of the electrode, as well as on the condition of the skin. Larger electrodes tend to have lower impedance and produce less noise [30]. The susceptibility to PLI of a sEMG-system is defined as common-mode rejection ratio (CMRR). This concept will be described in detail in chapter 4.1.1. A low electrode-skin impedance of the grounding electrode is reducing the common-mode present at the electrodes and a reduced electrode-skin impedance imbalance prevents the common-mode from being amplified.

2.2.3 Active Electrodes

Wearable sEMG devices use dry electrodes instead of disposable sticky electrodes, which are often used in clinical application. Dry electrodes result in higher skin-electrode impedance and therefore make the system more susceptible to powerline interference (section 2.2.2) [31]. To reduce the impact of the voltage divider effect (2.2.1) the electrodes are connected to a buffer stage with a high input impedance and a

low output impedance. This buffer stage acts as an impedance converter to prevent CMRR degradation. If the electrodes are close to the buffer stage, they are called "active" electrodes. The buffer stage is crucial to build a robust circuit against power line interference and high skin-electrode impedance [32].

2.2.4 Acquisition Modes

SEMG signal is always a voltage measured against a reference voltage. These differences in electric potential present at the skin are detected by a differential amplifier. There are different Acquisition modes depending on the referenced signal. Three different modes are found to be suitable for sEMG measurements: Single differential (SD), Double differential (DD), and Monopolar (MP) (Figure 2.7).

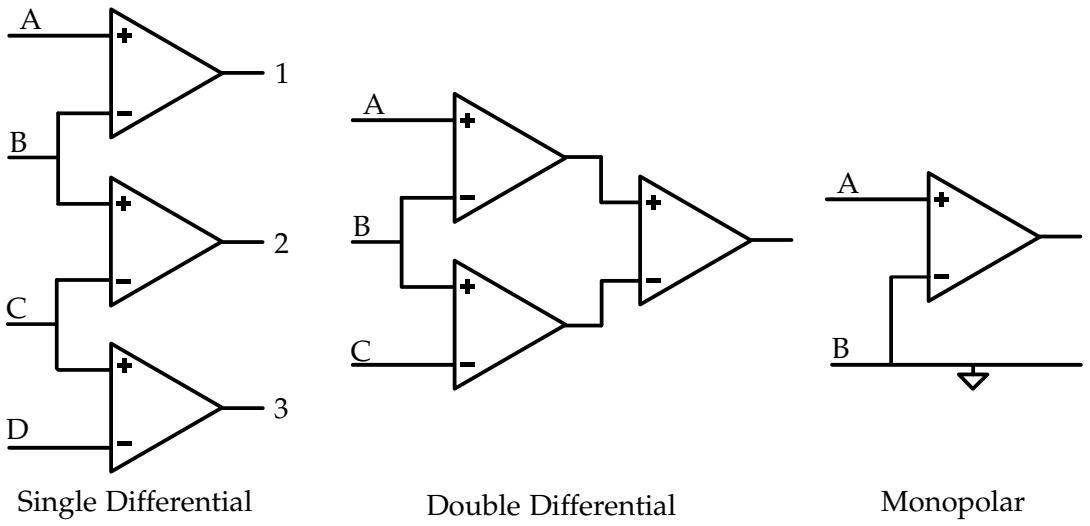

Figure 2.7: Simplified schematic of different acquisition modes in sEMG

Monopolar

In monopolar acquisition, each electrode records the electric potential at its site relative to a distant reference electrode, typically placed over an electrically inactive bony area. This configuration captures the global electrical activity of the underlying muscle but is more susceptible to cross talk and PLI than SD and DD.

Single Differential

Also referred to as Bipolar, SD acquisition is widely used in sEMG applications, particularly in wearable systems, because it eliminates the need for placing a reference electrode over a bony landmark, which can be challenging in wearable designs. In this mode, the detected signal is obtained by subtracting the voltage measured a one electrode from that at its neighbor. In a SD array, a signal can serve as input for multiple differential amplifiers (see Figure 2.7 B).

Double Differential

In double differential mode, the signal is acquired by calculating the difference between the single differential outputs from adjacent electrode pairs, mathematically expressed as:

$$V_{\mathrm{DD}} = (V_A - V_B) - (V_B - V_C) = V_A - 2V_B + V_C$$

The double differential mode selectively amplifies signals originating from motor units directly beneath the recording array while strongly suppressing distant or common-mode potentials. As demonstrated by Merletti et al., this approach increases sensitivity to motor unit action potentials that exhibit steep spatial gradients, thereby enhancing discrimination against crosstalk and background noise [33].

Detection Volume

The pick-up volume of an electrode configuration describes the region within the muscle from which detectable myoelectric activity can be recorded with a sufficient SNR. This volume depends on both the electrode geometry and the signal acquisition mode.

In monopolar recordings, the potential at each active electrode is measured with respect to a distant common reference. As a result, the recorded signal amplitude primarily reflects the absolute voltage generated by the MUAP at that site, regardless of the relative differences between neighboring electrodes. This allows monopolar configurations to capture signals effectively from both superficial and deep motor units. This increase in detection volume causes an increase in susceptibility to cross talk using a monopolar configuration.

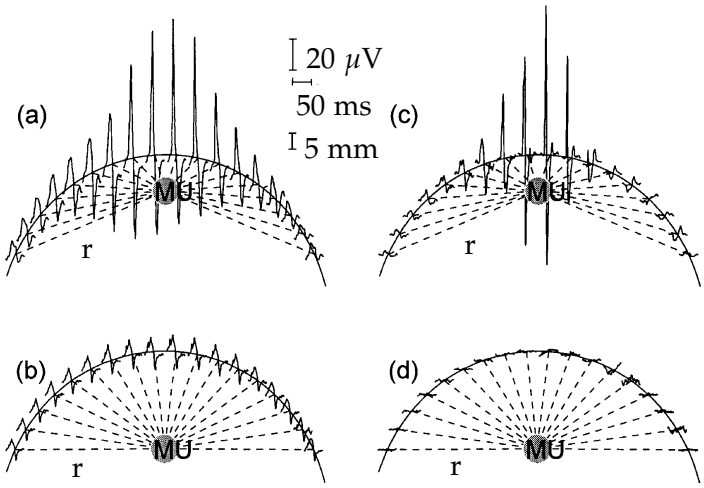

Figure 2.8: Cross-sectional views of superficial (a, c) and deep (b, d) motor units, simulated measurement with monopolar (a, b) and single differential (c, d) recordings at 18 sites across radial distances r from the motor unit. From [34].

In SD recordings, the signal is obtained by subtracting the potentials measured at two adjacent electrodes. This mode enhances spatial selectivity by suppressing common signals, but it also limits the detection volume. For superficial motor units, differences in radial distance between the source and each electrode result in distinct signal shapes and amplitudes, producing a strong differential signal. In contrast, for deep motor units, the variation in path length and amplitude between adjacent electrodes is minimal. Consequently, the subtraction yields a smaller differential signal, even though the monopolar components remain (Figure 2.8). Thus, SD recordings exhibit reduced sensitivity to deeper motor units compared with monopolar recordings, as their detectability depends on spatial voltage gradients rather than absolute amplitudes. This makes the SD mode less susceptible to cross talk from muscles further away from the detection site than monopolar acquisition mode. DD recordings show an even smaller detection volume and therefore higher spatial selectivity [35].

2.2.5 Cross talk

Cross talk, defined as the contamination of sEMG signals by electrical activities from neighboring muscles, is a significant challenge when interpreting sEMG measurements [36]. Especially in the context of intention detection, cross talk can result in misinterpretation of muscle activity, which subsequently lead to wrong movement predictions [37]. The forearm contains a dense array of small, closely packed muscles, many of them are

synergists or antagonists involved in fine motor control of the hand and wrist. Due to the limited spatial selectivity of sEMG electrodes, signals recorded from one muscles can include contributions from adjacent muscles.

Cross talk occurs primarily due to the volume conduction properties of biological tissue, where action potentials from active motor units spread through skin, fat, and connective tissue, reaching the electrodes placed over neighboring muscles [38]. Cross talk showed statistically significant increases with larger electrode contact areas and with increased IEDs [39]. Temporal filtering methods like band-pass filter are largely ineffective against cross talk, as its spectral characteristics (e.g. mean frequency) often overlap with those of the target muscle signals [38]. Instead spatial filtering techniques - such as single and double differential configurations - have been shown to reduce cross talk [40, 41]. Furthermore, Advanced signal processing methods such as inverse modeling showed to reduced cross talk in simulation tests [42] .

2.2.6 Electrode size and Inter-electrode distance

Physical dimensions of electrodes and the IED play a crucial role for different aspects of sEMG including susceptibility to cross talk, CMRR, SNR, and filtering. Especially dry electrodes used in wearable devices show an increase in electrode-skin impedance and noise levels [43]. Larger electrodes reduce the electrode-skin impedance and root mean square (RMS) noise of the signal but introduce a spatial filtering effect. This filtering effect causes an attenuation of high-frequency spatial components by averaging the potential over a wider area [44]. Additionally larger electrodes reduce the spatial density of the sEMG-system.

Investigations of high-density surface electromyography (HD-sEMG) showed that denser grids - realized with small electrodes (1 mm diameter) and reduced IED (4 mm) - increased the number of identifiable MU [45]. Identification of single MU gives additional insights about muscle activity, including firing patterns and recruitment.

Accurate spatial reconstruction of sEMG signals requires spatial sampling that meets the Nyquist criterion: at least two samples per wavelength are necessary to reconstruct the signal without aliasing [44]. Practically, this means the minimum detectable spatial wavelength is twice the electrodes spatial resolution or IED. For a grid with an IED of 5 mm, the minimum wavelength is 10 mm. Considering a CV of 5 m/s, this corresponds to frequency of 500 Hz. Figure 2.9 depicts the transfer function of two circular electrodes for different IED. The transfer function combines the effect of electrode size and IED on how a signal is attenuated dependent on its frequency, size of used electrode, and IED. For example: A signal with a frequency of 500 Hz and a CV of 5 m/s will not result in any signal at two differential electrodes with an IED of 10 or 20 mm because its wavelength is a multiple of the IED. Additionally Figure 2.9 shows that signals with

a CV of 4 m/s and a frequency < 50 Hz are attenuated stronger than signals with a frequency of 50-100 Hz. The influence of IED, electrode size on the transfer function need to be considered when analyzing signals from sEMG systems.

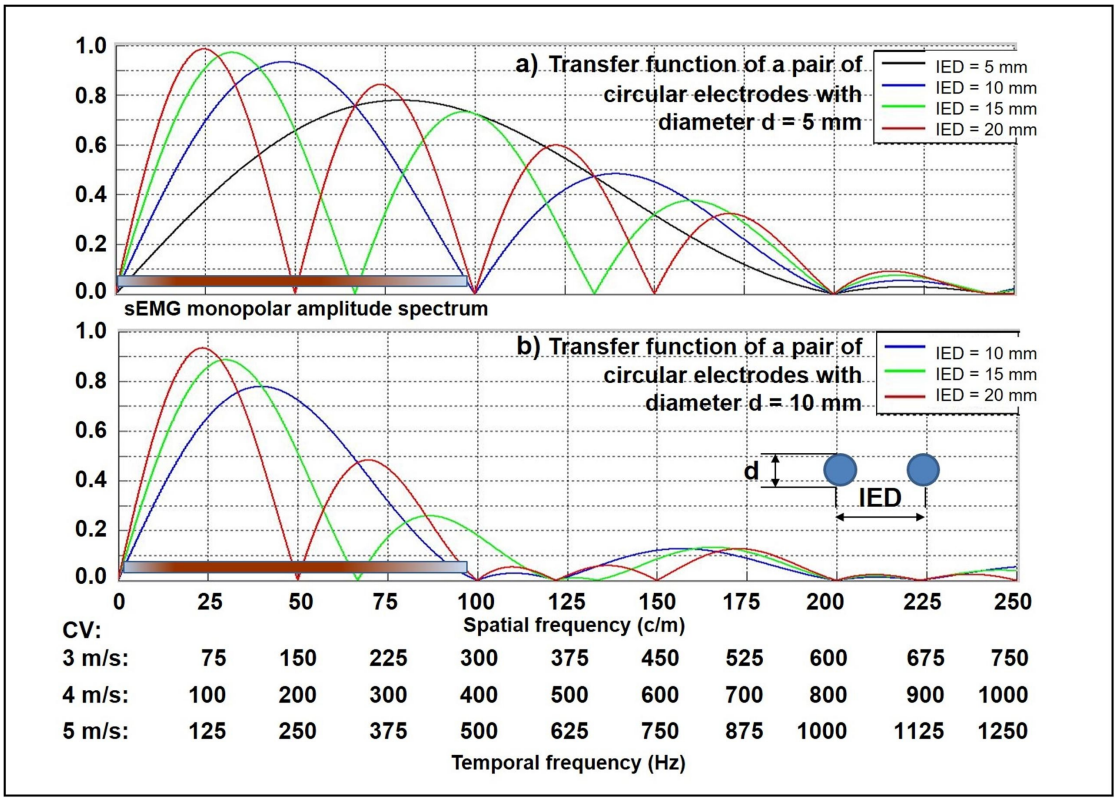

Figure 2.9: Combined transfer functions of two circular electrode sizes (5 mm in a, and 10 mm in b) and different inter-electrode distances: 5 mm, 10 mm, 15 mm, and 20 mm. The monopolar sEMG amplitude spectrum bar is represented with color intensity to indicate the relative strength of its harmonic components. The corresponding temporal frequency to the spatial frequencies can be obtained by scaling by the conduction velocity CV. From [46]

A critical trade-off emerges when designing electrode arrays for sEMG: larger electrodes and sparser grids reduce noise and skin-electrode impedance effects but increase spatial filtering that attenuates high-frequency signal components [47]. Conversely, denser grids with smaller electrodes enhance spatial resolution and preserve signal details, which is beneficial for motor unit discrimination and decomposition, but tend to be more susceptible to higher noise levels and variability in skin impedance [48].

2.2.7 Driven Right Leg Circuit

The driven right leg (DRL) circuit is a form of active grounding in biomedical signal acquisition, such as sEMG and electrocardiography (ECG), designed to increase the CMRR.

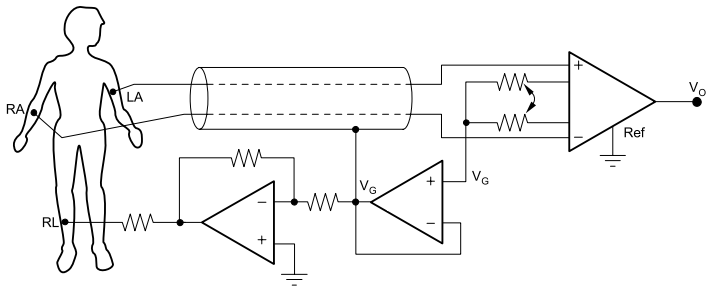

Figure 2.10: Simplified schematic of a driven right leg circuit. Adapted from [49].

The DRL circuit reduces common-mode noise by detecting the common-mode voltage at the amplifier inputs. It amplifies, inverts this signal and feeds it back into the patient's body via a dedicated electrode (Figure 2.10) [50]. This electrode is usually placed at an electrically neutral site such as the right leg.

3 State of the Art

This chapter reviews the evolution of sEMG wearables, beginning with early low-density wristbands developed for gesture control, progressing to advanced high-density research devices, and also presenting two established commercial EMG systems widely adopted as clinical and research reference standards. Key distinctions between these systems - including electrode configurations, materials, and sample rate - are explored in the context of their target applications.

3.1 Myo armband from Thalmic Labs

Myo armband (Figure 3.1) from Thalmic Labs was the most widely adopted commercial, non-invasive EMG interface for wearable gesture and motion recognition applications, before its discontinuation in 2018. It represented the a common platform for testing classification algorithms for intention prediction. The Myo armband featured 8 single differential modules each containing 3 dry stainless steel electrodes. These electrodes are rigid, rectangular bars each with a contact area of 10 x 10 mm . The modules are distributed equidistantly at 45-degree intervals in a single axial ring, covering the major flexor and extensor muscles groups in the forearm. The EMG signals are digitized by an 8-bit analog-to-digital converter (ADC) at a fixed sampling rate of 200 Hz per channel [2].

In addition to EMG sensing, the device incorporates a 9-axis inertial measurement unit (IMU), enabling detection of forearm/wrist kinematics [51].

Figure 3.1: Myo Armband from Thalmic Labs with 8 sensor modules and 200 Hz sample rate [3].

The Myo armband was engineered as a cost-effective, easy-to-use wearable platform for EMG-based gesture recognition, and a variety of human machine interface applications. Its commercial success was largely due to its straightforward, gel-free electrode design and robust wireless data streaming, enabling rapid deployment in both research and consumer context [52].

The Myo armband shows several limitations. Its sampling rate of 200 Hz restricts frequency detection to a maximum of 100 Hz according to the Nyquist criterion. Since surface EMG signals typically span up to 500 Hz, a significant portion of the frequency spectrum remains unrecorded. Additionally, the device's low spatial resolution, with only eight sensor modules, is insufficient to capture the complex muscular activity within the human forearm [53].

3.2 Reality Labs Research Wristband

Following the discontinuation of the Myo armband production, North (formerly Thalmic Labs) sold its relevant patents to CTRL Labs, a neural interface startup and they developed the CTRL-Kit. In 2019, Meta (then Facebook) acquired CTRL-Labs to accelerate their own advancements in wearable neuromotor interfaces. This section is based on an article published by Meta that introduces the research wristband [54].

The sEMG research device (RD) by Reality Labs (Meta) is a sEMG wristband based on the CTRL-Kit by CTRL-Labs.

Figure 3.2: Rendering of the sEMG RD by Meta [55].

Unlike the Myo armband, Reality Labs' research wristband features 16 single differential modules, each containing 3 gold-plated brass electrode pins (Figure 3.2). For each module, two pins are used for single differential/bipolar signal detection, while the third one is serving as a shielding and grounding electrode. The combined electrode design improves skin contact and comfort during use. The module's inter-electrode distance is fixed at 20 mm, with each circular electrode providing a contact area of approximately 33 mm (diameter: 6.5 mm). This spacing exceeds the optimal spatial bandwidth of sEMG signals (typically 5-10 mm), limiting spatial resolution as described by Farina et al. [56] and further detailed in Subsection 2.2.6.

Comparable to the Myo armband, the sEMG RD incorporates a 9 axis IMU to capture wrist and forearm kinematics. The input impedance of the analog front-end is approximately 10 TΩ resistance in parallel with a 10 pF capacitance, ranking among the highest for research-grade wearable sEMG devices. The high input impedance increases CMRR (see section 2.2.2). The sampling rate can reach up to 2 kHz, providing the temporal resolution to detect signals across the entire sEMG frequency spectrum of MUAPs for different CVs (Figure 2.9).

Gesture recognition is performed using advanced machine learning models, trained on large-scale user datasets, and shows strong generalizability to anatomical differences and calibration-free operation [54]. Ongoing development focuses on miniaturizing the device, targeting watch-like form factors suitable for augmented reality applications, particularly within entertainment and human-computer interaction domains. To this day, the Meta wristband is not commercially available.

3.3 Neubond

Neubond wristband (Figure 3.3), developed by the Imperial College London spin-out Neubond, is a wearable neuromuscular interface designed primarily for stroke rehabilitation and neuroplasticity-based recovery. Intended as a clinical and home-use solution, the Neubond device features a high-density array of miniaturized electrodes embedded around a flexible forearm cuff. These electrodes detect sEMG signals associated with muscle activation during intended movements, enabling capture of user intention [57]. Compared to the Myo armband, Neubond employs smaller electrodes and a shorter IED, which increases spatial resolution and reduce filtering effects.

Figure 3.3: Rendering of the Neubond Wristband. From [58].

Unlike many research wristbands, Neubond claims that the system provides targeted, on-demand stimulation to corresponding nerves and muscles, reinforcing the connection between motor intent and neuromuscular execution [59].

The Neubond wristband comprises presumably 12 single differential electrode modules combined with integrated stimulators and delivers not just monitoring, but also interactive feedback to enhance rehabilitation outcomes. Pilot clinical tests with stroke patients showed improvements in voluntary control, muscle activation amplitude, and functional abilities such as grip strength and dexterity.

3.4 Ottobock 13E200

The Ottobock 13E200 (Figure 3.4) is an established bipolar EMG sensor module used widely in prosthetic control and as a reference system for new research EMG sensors [60], [61]. The electrodes are manufactured from titanium to ensure biocompatibility. The two outer electrodes function as inputs for bipolar signal detection, while the larger central electrode serves as the grounding reference. The sensor incorporates an analog front-end with integrated amplification and filtering circuitry, embedded

in a robust housing. The sensor module measures 27 mm in length, 18 mm in width, and 9.5 mm in height, weighing approximately 4.5 g. This widely used sEMG system has even been employed to create an armband for controlling a hand prosthesis [62]. The increased IED compared to the Neubond and recommendations from leading researchers (maximum 10 mm, see section Subsection 2.2.6) limits the performance and presents opportunities for improvement.

The Ottobock13E200 were specifically developed for prosthetic control within the MyoBock system.

Figure 3.4: Ottobock 13E200 Bipolar electrode for control of prosthetics. From [63].

3.5 Quattrocento from OT Bioelettronica

The Quattrocento (Figure 3.5) is a high-channel-count desktop bioelectric amplifier developed by OT Bioelettronica for multi-channel sEMG and electroencephalography (EEG) acquisitions. It supports up to 400 channels, with multiple selectable versions tailored for diverse laboratory and research applications.

Figure 3.5: Rendering of the OT Bioelettronica Quattrocento desktop bioelectrical amplifier. From [64].

The device employed as a reference system in EMG research, including for testing new sensor designs, validating decomposition algorithms, and comparing electrode configurations [65], [45], [66], [67], [68].

The analog to digital conversion is performed using 24-bit ADCs, which provide a broad dynamic range for precise signal digitization - a specification which the Quattrocento can sustain, in contrast to wearable devices where power and communication constraints typically necessitate lower resolutions, such as 12-bit. Sampling frequencies are configurable, enabling selections such as 512 Hz, 2048 Hz, 5120 Hz, and 10 240 Hz, thus allowing flexible temporal resolution adapted to the EMG acquisition task. Band-pass filtering can be configured to 0.7-200 Hz for the high-pass filter and 130-4400 Hz for the low-pass filter. The Quattrocento device supports Ethernet and USB interfaces for robust data transfer, and includes sixteen auxiliary input channels and one analog output for synchronization with external devices.

4 Methods

To achieve the research aim this thesis should comprise the design and validation of a customizable EMG-Sensor module for the DLR research wristband. The requirements and validation procedures of each subsystem are divided in a V-Model (Figure 4.1).

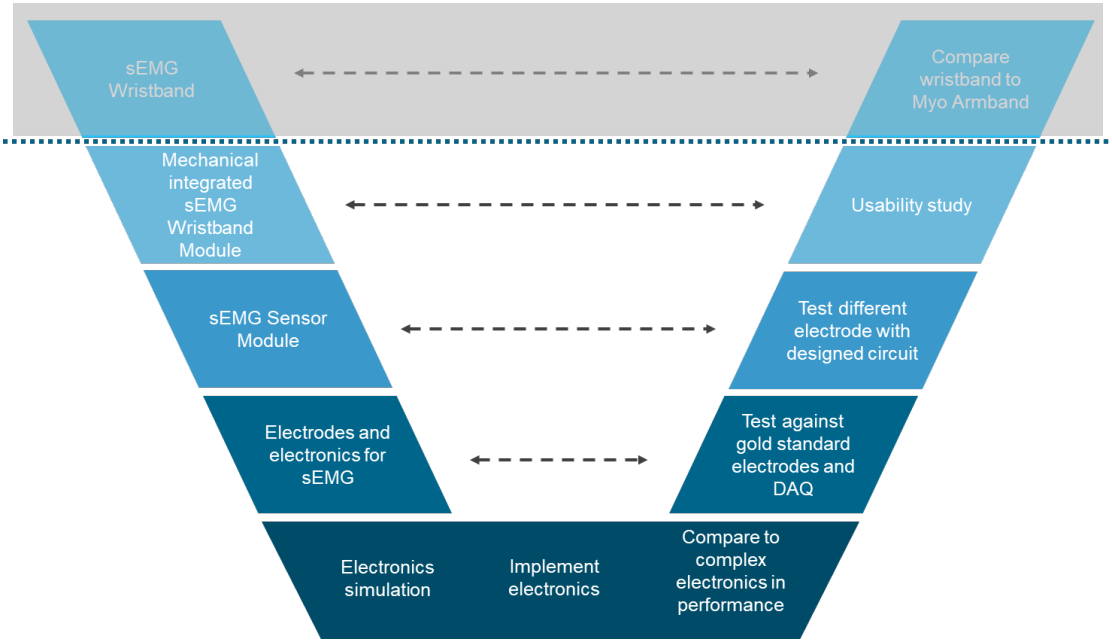

Figure 4.1: V-Model for Design and Validation of a sEMG Module

Validation tests at each milestone ensure subsystem requirements are met and design progress is documented.

4.1 Simulation

The first step of the V-Model includes a Spice simulation of the electronic circuit, where signals of the electrodes are filtered and amplified. High-quality sEMG signal

acquisition requires a functional circuit. Essential tasks include signal amplification, filtering, and common-mode voltage reduction. The capabilities of the designed circuits are validated through simulation and comparison with state-of-the-art hardware.

4.1.1 Design of the Simulation Circuitry

Four circuits were designed and simulated:

Single differential with three electrodes	(SD3EL)
Single differential array with six electrode	(SD6EL)
Double differential with four electrodes	(DD4EL)
Monopolar array with six electrodes	(MP6EL)

One electrode is serving as a grounding reference in every circuit. The simulation of each of the four circuits can be divided into four functional blocks (Figure 4.2): the input stage, the electrode–skin interface, the amplification stage, and the analog filter and bias circuitry. The input stage comprises the simulated EMG signal, noise sources, and the common-mode component. The Amplification, Filter, and Bias parts form the designed sEMG circuit. Acquisition modes are implemented within the amplification stage, while the remaining blocks are identical for all circuit configurations.

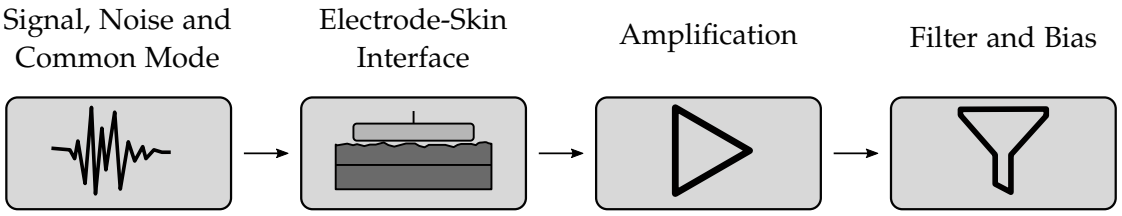

Figure 4.2: Parts of the sEMG simulation

The muscle signal displays stochastic amplitude characteristics that can be approximated by a Gaussian distribution. Its amplitude typically ranges from 0 to 10 mV peak-to-peak or 0 to 1.5 mV RMS, with the RMS in this simulation set to 1 mV to resemble a typical physiological signal [21]. The usable spectral content lies between 0 and 500 Hz, with most energy concentrated in the 50 to 100 Hz band. Usable spectral content refers to the signal above the noise floor. For the simulation of the designed circuits, a muscle signal was generated as a Gaussian white noise band-pass filtered be-

tween 10 and 350 Hz, producing a time-domain waveform and corresponding frequency spectrum as shown in Figure 4.2.

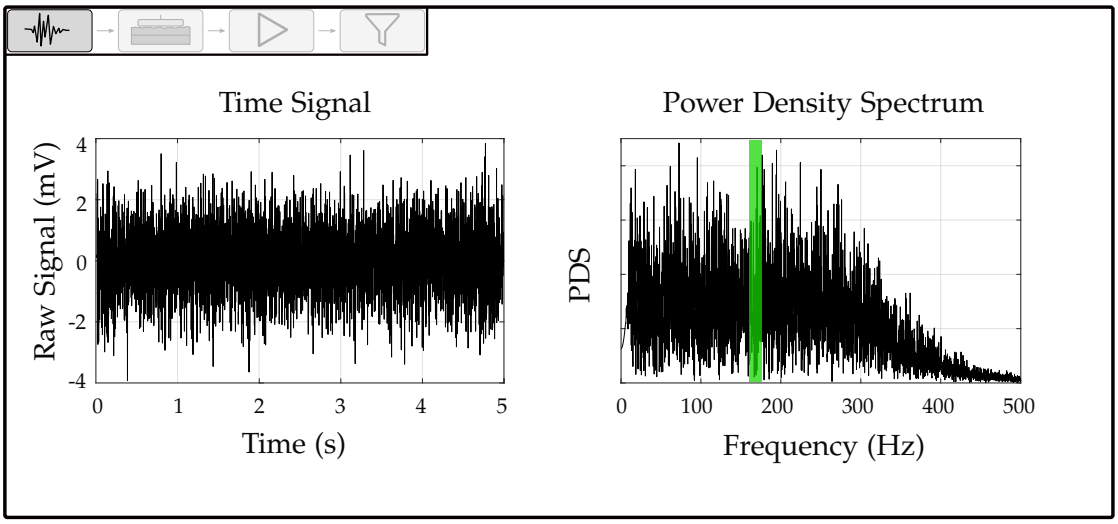

Figure 4.3: Simulated Muscle signal with a RMS of 1 mV and its frequency spectrum with a mean frequency of 167 Hz

Before the signal reaches the inputs of the EMG sensory circuit, it passes the simulated electrode-skin interface, which introduces an impedance. The electrode-skin impedance ranges between $10^3\Omega$ and $10^7\Omega$ [30].

The difference in skin-electrode impedance cause amplification of the common-mode voltage through the voltage divider effect (Subsection 2.2.2). Since the variations in skin-electrode impedance mainly arise from different sizes and materials of the electrodes, the skin-electrode impedance was be modeled in the simulation using an simplified version of the circuit model from Murphy et al. [69]. This version is a combination of a resistor in series with a RC parallel element with values of 950 k$\Omega\pm$10 % and 15 nF$\pm$10 % (Figure 4.4). These values represent an impedance of $|Z| \approx 975\,\text{k}\Omega$ at 50 Hz [30].

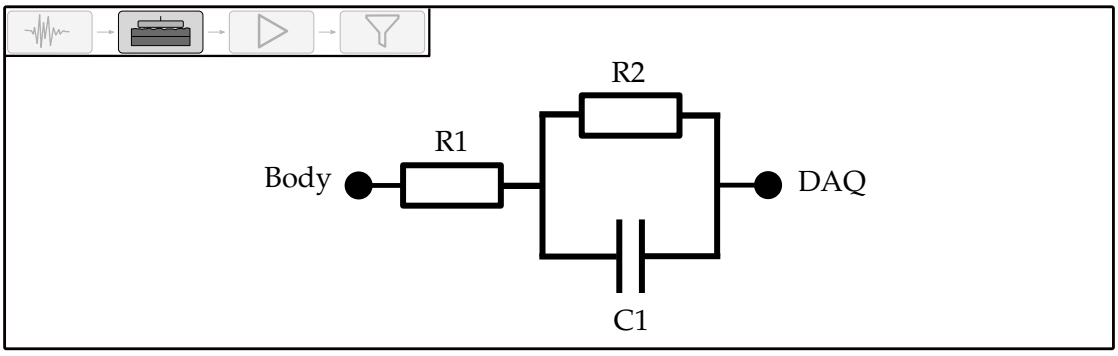

Figure 4.4: Skin-electrode interface circuit. Simplified version derived from [69]. Data acquisition (DAQ)

The sEMG sensor circuits start with an amplification stage (Figure 4.5), in which the voltages of two inputs from two electrodes are subtracted and multiplied by a factor. The amplification factor (gain) is depended on the Resistors R4 and R5. The values of the resistors are adjusted to amplify the simulated muscle signal that the highest peak of the output signal is below the saturation voltage (1.65 V). Due to space constraints, wearable devices often omit the DRL circuit, as its additional components can complicate compact designs. Instead of using active grounding as in the DRL, all designed sensor circuits - except for the monopolar configuration - employ a direct grounding method combined with a high-pass filter (C1, C2, C3, R1, R2, R3, Figure 4.5). This approach has been shown to achieve a level of common-mode noise reduction comparable to that of DRL circuits [70]. In the monopolar sensor circuit, resistor R1, R2, R3 and capacitors C1, C2, C3 are omitted, while resistors R4 and R5 are replaced by a single resistor to further minimize component count (Figure 4.5). In the MP6EL circuit, one reference electrode is connected to the negative input of all amplifiers (Figure 2.7, Monopolar). An additional buffer stage is implemented in the MP6EL circuit to reduce the voltage divider effect (2.2.1), which is higher in the monopolar configuration because the reference electrode is used as an input for all amplifiers. In the DD4EL circuit a second differential stage with a gain of 1 is employed with outputs of the first stage serving as inputs (Figure 2.7, Double Differential).

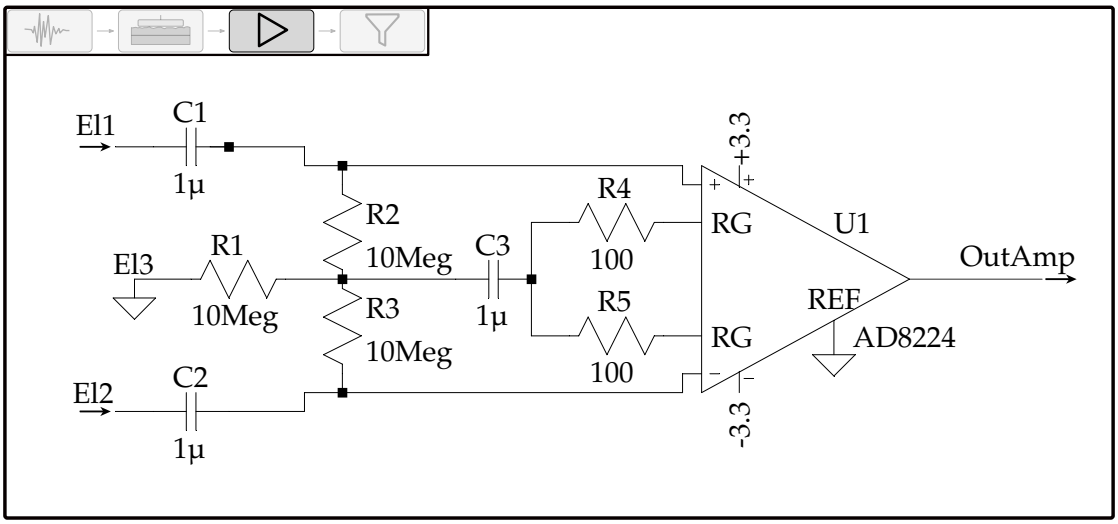

Figure 4.5: Differential amplification stage with a gain of 248 and a direct grounding approach after [70].

The amplified signal is band-pass filtered using a second-order active high-pass Sallen-Key filter followed by a second-order active low-pass Sallen-Key filter and then shifted to half the supply voltage to accommodate the ADC, which accepts only positive input voltages (Figure 4.6). The band-pass filter consists of a high-pass stage with an 11 Hz cutoff frequency and a low-pass stage with a 503 Hz cutoff frequency. This filter design is adapted from Polo et al. with modified component values for easier procurement, while still effectively covering the relevant frequency range for sEMG signals [71], [72].

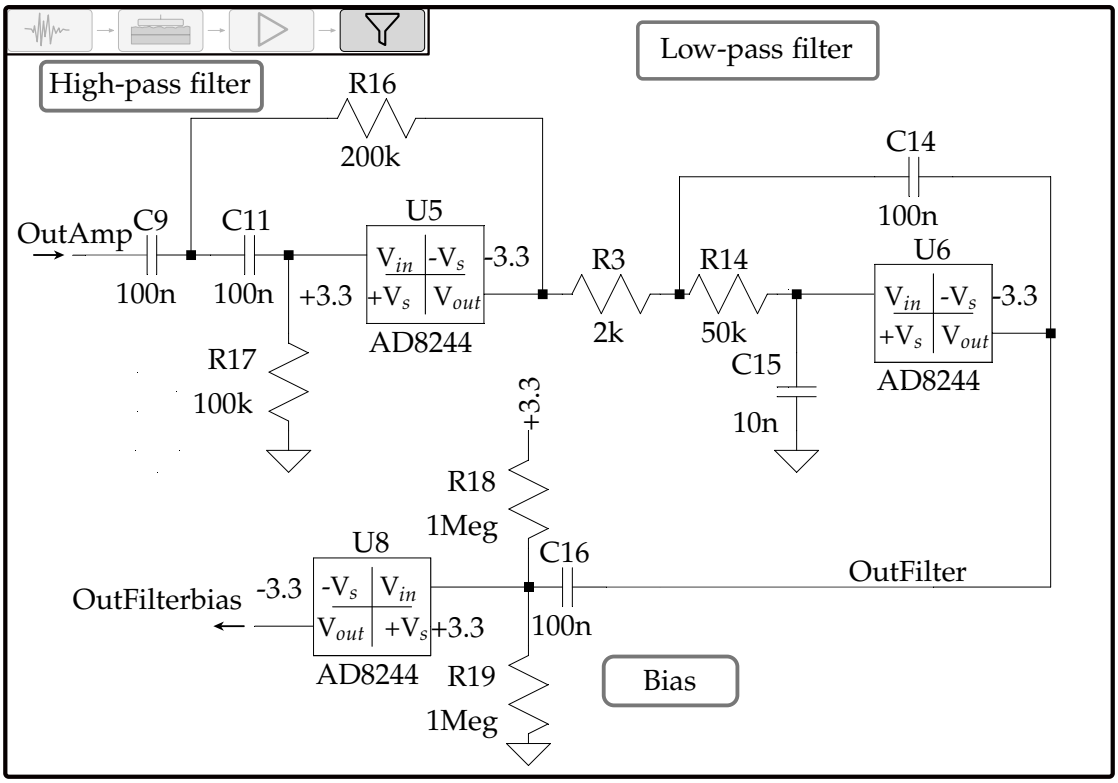

Figure 4.6: Filter and bias circuits including a Sallen-Key band-pass filter adjusted from [71] and a bias circuit to add half the supply voltage to the signal.

4.1.2 Test Procedure

The simulation was carried out in LTSpice, version 17.1.15 (Analog Devices, USA). In order to test the circuit functionality, inputs of the simulation include noise introduced by the skin electrode interface, PLI voltage, and the sEMG signal. The input muscle signal is delayed by 0.0025 s between the electrodes to account for the propagation time. This time delay of $\Delta t = 2.5$ ms was calculated assuming a CV of 4 m/s and an inter-electrode distance of 10 mm [73].

In Table 4.1 the functions for the input of the simulations are stated. Signal, Common-Mode, and Noise (Rows of Table 4.1) were connected to the inputs of the circuit depending on what criteria to test. Outputs and inputs of the simulation were measured over of 4 s to have a sufficient duration for frequency investigations. The gain of the amplifier was be calculated numerically using the formulas found in the data sheet of the components. The total gain in the simulation was calculated by comparing the RMS

Table 4.1: Simulation inputs at each electrode. MS: Muscle signal, Signal (t): Simulated muscle signal, Δt = 2.5 ms, CM: Common-mode

	Electrode 1	Electrode 2	...	Electrode 6
MS [mV]	signal(t)	signal($t + \Delta t$)	...	signal($t + 5\Delta t$)
CM [V]	$0.6 \sin(50\,\text{Hz} \cdot t)$			
Noise [µV]	10 VRMS white noise			

value of the EMG signal input and the RMS of the output signal when only the muscle signal is used as input and not the PLI or noise. The gain of the common-mode voltage was calculated analog: PLI is introduced into the circuit but no muscle signal and the RMS values of the output is divided by the RMS value of the input. The CMRR was calculated by following formula:

$$\text{CMRR} = 20 \cdot \log_{10}\left(\frac{A_d}{A_{cm}}\right)$$

A_d is the gain or amplification of the differential signal, in this case the electric signal from the muscles, and A_{cm} describes the gain on the common-mode signal, in this case the interference from the power line. CMRR was calculated for every circuit, once with an equal electrode-skin impedance and once with a 10 % imbalance. The SNR depends on the noise introduced at the circuit input and reflects a the same performance aspect as the CMRR. In the simulation, the common-mode component is known, allowing direct calculation of the CMRR. In a real-world measurement, this is not feasible. Therefore, the SNR is used as the primary criterion to evaluate circuit performance in practical measurements, but not in the simulation.

4.1.3 Validation Criteria

The two primary criteria tested in the simulation are the CMRR and the amplification factor (gain). The CMRR is critical, as poor common-mode rejection is one of the major challenges in sEMG signal acquisition. The gain must be sufficiently high to ensure adequate output signal amplitude, yet limited to avoid saturation of the amplifiers and ADC. The total gain of the sEMG system is divided into four individual amplification transfer functions (Figure 4.7). The electrode is acting as low-pass filter dependent on the contact area. Gain variations across the sEMG relevant frequency are negligible for the amplifier stage. Differential measurements introduce a frequency-dependent gain dependent on the IED. A combination of the electrode and differential transfer function is shown in Figure 2.9.

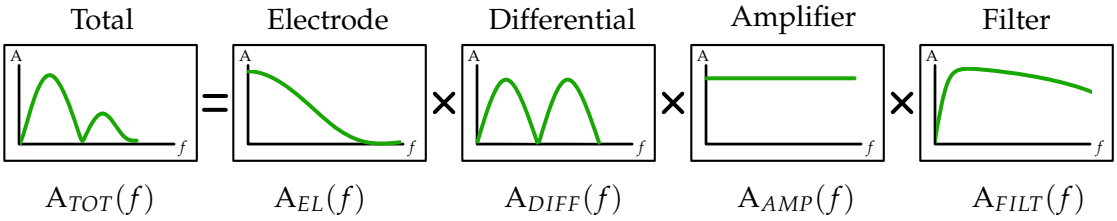

Figure 4.7: Frequency-dependent gain characteristics of different stages in the sEMG system.

Validation parameters were validated by comparing the simulated results with values reported in the literature. Although not evaluated in the simulation, the physical dimensions of the circuitry influenced the circuit design for the simulation, as the footprint of the components must meet space constraints.

4.2 Isometric Contraction Test Protocol

A testing protocol was developed for testing different electrodes and sensor configurations. This protocol was consistently applied across all human subject trials to establish a comparable data set. The biceps brachii, referred to as biceps in this thesis, was chosen due to its size minimizing cross talk from adjacent muscles and ensures that all sensors can be placed over one muscle. Electrode positions were documented to enable reproducibility and maintain consistent sensor placement throughout the study.

To ensure consistent muscle contractions, the subject positioned the upper arm on an angled profile, while the lower arm was held horizontally, resulting in an elbow flexion angle of approximately 30° (Figure 4.8). The protocol comprises six trials with sequentially added weights to the hand. Each trial involves a 7-second isometric contraction, during which 5 seconds are recorded to exclude the initial lifting phase and the final release. The first measurement is a baseline reference during which the subject fully relaxes the arm. Loads ranged from 1 kg up to 6 kg, increasing in 1 kg steps. This upper limit was selected to represent a typical load encountered in daily activities, such as carrying a six pack of water.

After each trial, rest periods were provided as needed to prevent muscles fatigue. The test sensor was positioned between the center of the muscle and the muscle-tendon junction, provided the sensor was not too large, in order to avoid the innervation zone. Its important to note, that the innervation zone can be different across applied loads [74]. Therefore, a possibility remains that the sensor is positioned above the innervation zone. This potential variability should be considered when evaluating results.

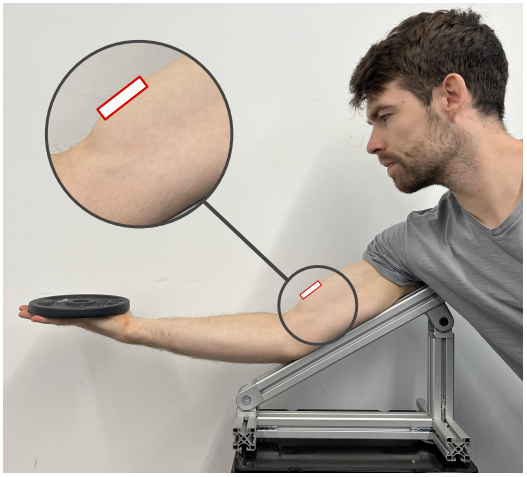

Figure 4.8: Person positioned according to the test protocol with a indicated sensor position.

4.3 Electrodes and Circuitry

The second step of the V-Model includes two subsystems: The electrodes and the analog circuitry each within a printed circuit board (PCB). Each electrode is compared to widely used hydrogel electrodes connected to a Quattrocento system (OTBioelettronica, Turin, Italy). The analog circuitry is validated by verifying the total gain across different frequencies and comparing SNR of the circuit and the Quattrocento. Both systems use the same electrodes to secure comparability.

4.3.1 Design and Construction of Electrode and Circuitry

The sensor circuitry and the electrodes are designed in stacking configuration to enable connecting different electrodes to the same circuit (Figure 4.9).

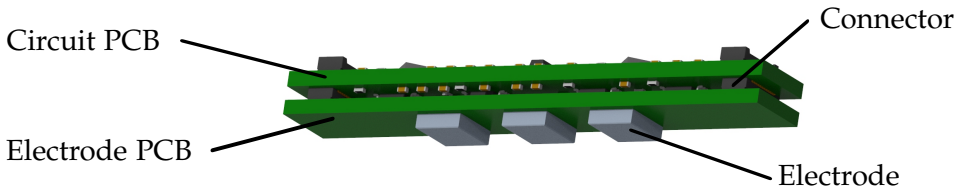

Figure 4.9: Rendering of SD3EL Sensor Module in a stacked configuration.

Three distinct electrode PCBs were designed. The first, designated as 3EL, is used with the SD3EL configuration and features three electrodes with a 10 mm IED. The second PCB, referred to as 4EL, accommodates the DD4EL circuit with four electrodes, also with an IED of 10 mm. The third, labeled 6EL, is compatible with both the SD6EL and MP6EL configurations and contains six electrodes with an 8 mm IED. The electrodes have a rectangular contact area with a size of 5 x 6 mm and are made from stainless steel. The lower IED for the 6 electrode configuration allows to fit 6 electrodes in the same module dimensions. The contact area reflects a compromise between reducing noise, ensuring a low impedance skin-electrode interface with a large electrode and an acceptable low-pass filtering due to the size of the electrode (Subsection 2.2.6).

The electrode material is a medical degree stainless steel (1.4301), chosen for its biocompatibility, corrosion resistance, and affordability. Electrodes are fixed to the PCB using conductive silver epoxy glue 8331D from MG Chemicals (Burlington, ON, Canada). A gluing template ensured accurate electrode positioning and IED (Figure 4.10). While the glue was drying, the electrodes were pressed onto the PCB using a weight. Each electrical connection between an electrode and its corresponding PCB pin was tested for resistance introduced by the adhesive. Connections with a resistance below 1 kΩ were considered acceptable, as this is negligible compared to the much higher skin–electrode impedance variance.

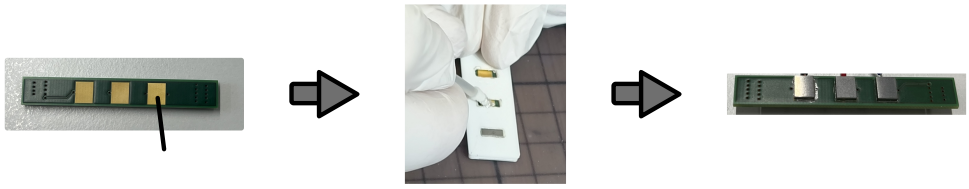

Figure 4.10: Assembly process of electrode PCB.

The active components of the circuits were selected with consideration of input impedance, CMRR, power consumption, and packaging size to optimize circuit performance and reliability. The amplifier in a sEMG circuit has a direct impact on critical characteristics such as CMRR, gain, and noise performance, leading to the choice of an instrumentation amplifier (IA) with an integrated buffer stage and compact package.

The input impedance of the IA is a critical feature because the magnitude of the Noise due to PLI in inversely proportional to the input impedance of the IA (see 2.2.2). Table 4.2 compares various IAs, highlighting favorable characteristics in green and the ones leading to exclusion in red. The AD8224 (Analog Devices, Wilmington, MA, USA) was selected due to its high input impedance, compact footprint, and compatible

operating voltage. In simulations, the AD8224 demonstrated a 90 % reduction in PLI susceptibility compared to the AD8422 (Analog Devices, Wilmington, MA, USA), demonstrating the impact of higher input impedance and justifying its higher power consumption. The AD8235 showed the most promising properties but cannot handle negative inputs and is therefore not suitable for sEMG front-end applications.

Table 4.2: Comparison of Instrumentation Amplifiers for sEMG applications

	Instrumentation Amplifier						
Parameter	**AD623 [75]**	**AD8422 [76]**	**INA333 [77]**	**AD8224 [78]**	**LTC6373 [79]**	**AD8220 [80]**	**AD8235 [81]**
CMRR (G>100)	>105 dB	>126 dB	100 dB (G>100)	>100dB (G>100)	>103 dB	100dB	>120dB
Input Impedance GΩ ‖pF	2‖2	200‖2	100‖3	10000‖5	10000‖6	10000‖5	440‖1.6
Power Consumption	550μA max	368μA max	75 μA max	800μA max	750μ max	750μA max	40μA max
Voltage Noise Density	35 nV/$\sqrt{\text{Hz}}$	8 nV/$\sqrt{\text{Hz}}$ (max)	50 nV/$\sqrt{\text{Hz}}$	17 nV/$\sqrt{\text{Hz}}$	8 nV/$\sqrt{\text{Hz}}$ (max)	76 nV/$\sqrt{\text{Hz}}$	76 nV/$\sqrt{\text{Hz}}$
Package	-	single 3x3 mm	-	dual 4x4 mm LFCSP	3x5 MSOP	3x5 MSOP	1.6x2 mm 11 ball
Note	-	-	commonly used	-	Maximum Gain of 16	Fully integrated ECG circuit	operating range 1.8–5.5 V

The AD8244 operational amplifier (op-amp) is employed in the filter and bias stage, which requires three op-amps. The AD8244 quad op-amp (Analog Devices, Wilmington, MA, USA) provides four high-performance op-amps within a compact package and is recommended for Sallen-Key filter applications [82]. Due to its high input impedance, the AD8244 can also be used as a buffer in the MP6EL circuit.

A voltage converter, although not directly affecting the signal, is essential for amplifying sEMG signals. The sEMG signal can be partly or fully negative, requiring IAs to handle negative input voltages. To accommodate this, the amplifiers need a negative supply voltage rather than only a ground reference. The voltage converter TPS60402 (Texas Instruments, Dallas, TX, USA) meets this requirement by converting 3.3 V to -3.3 V, providing the necessary negative supply voltage for the IAs [83].

4.3.2 Electrode and Circuitry Validation Setup

Circuitry

To evaluate gains (A_{tot}, A_{filt}) and SNR independently of human variability, a validation trial was performed using a generated voltage source. The digital oscilloscope DHO924S (RIGOL Technologies, Suzhou, China) served as a signal generator to produce a sinusoidal waveform with constant amplitude and frequency. Evaluation boards were connected to the top and bottom sides of the analog circuit boards, enabling the introduction of the test signal via a probe with series resistance of less than 1 Ω.

The Analog output was measured using the RedLab 1208FS-PLUS (Meilhaus Electronic, Alling, DE) at a sampling rate of 2000 samples per second. This data acquisition device provides 12-bit resolution on single-ended or differential inputs across a 0-20 V range, equivalent to a least significant bit (LSB) $\approx$ 5 mV. Data post-processing was performed in MATLAB 2024 B (The MathWorks, Natick, MA, USA).

For comparison with an established sEMG system, the Quattrocento with an AD16 adapter was used in combination with the OTBiolab24 software. The sample frequency was set to 2048 Hz to account for the Nyquist criterion (see end of section 2.1). The signal probe was connected to input pin 1 of the AD16, while the generator ground was connected to pin 2 and both the input reference of the AD16 and the patient reference of the Quattrocento (Figure 4.11 (a)). The AD16 allows for measurements of 16 monopolar or 15 SD signals. SD acquisition mode is implemented digitally, resulting in no measurable SNR difference between the monopolar and DL configuration in this setup. According to the user manual, the Quattrocento system provides a fixed analog gain of 150 V/V, and OTBiolab24 applies additional conversion factors, thus making a direct gain comparison not feasible. Consequently, gain measurements were performed limited to the designed circuit to verify if the target gain is achieved.

Three different frequencies were tested (30, 70, and 170 Hz) in combination with 3 different amplitudes (2, 5, and 10 mV) to assess if the gain is dependent on the frequency. Although the circuit uses differential measurement, the signal is not truly differential. The waveform is only applied to one input, while the other input is referenced to ground, not the delayed signal as in the simulations. In the designed circuits (SD3EL, DD4EL, and SD6EL), signals were introduced to input 1 and therefore connected to one amplifier to produce 1 output signal (Figure 4.11 (b)).

For each introduced frequency and amplitude, both RMS and FFT analyses were performed. From the magnitude spectrum, the peaks at the test signal frequency and at 50 Hz (PLI) were compared to determine the SNR. In these generated input tests, SNR_{norm} is defined as the ratio of the magnitude at introduced signal frequency to the magnitude at PLI frequency (50 Hz). The magnitude of the signal frequency is normalized across input amplitudes to compare SNR_{norm} across different amplitudes

of the generated signals.

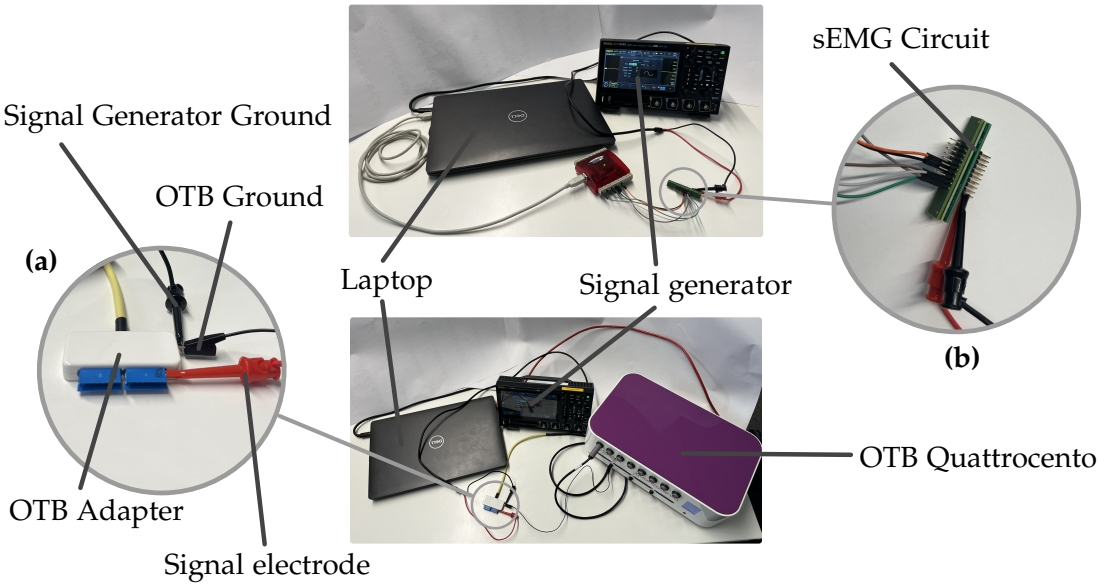

Figure 4.11: Test Setup for comparison between Quattrocento and designed circuits with generated inputs. Top: Designed circuitry. Bottom: Quattrocento sEMG reference system

A secondary comparison between the designed circuits and the Quattrocento reference system was performed in a single-subject study to assess the analog acquisition of sEMG signals. The test utilized CDE-S hydrogel electrodes (OTBioelettronica, Turin, Italy) with a diameter of 24 mm (Figure 4.12). These electrodes provide low skin-electrode impedance (<1 kΩ) due to their large surface area and conductive properties, making them well suited for evaluating SNR differences across circuits independently of electrode type [84]. However, the relatively large size of the electrodes and the IED of 25 mm imposes a limitation by inducing low-pass filtering effects and influencing the differential measurement transfer function (see section 2.2.6).

Measurements were carried out following the protocol outlined in Section 4.2. The SNR was calculated using the formula:

$$\mathrm{SNR} = 10 \cdot \log_{10}\left(\frac{\mathrm{Signal}_{eff,RMS}}{\mathrm{Noise}_{RMS}}\right) \tag{4.1}$$

with:

$$\mathrm{Signal}_{eff,RMS} = \sqrt{\mathrm{Signal}^2_{tot,RMS} - \mathrm{Noise}^2_{RMS}}. \tag{4.2}$$

The Noise$_{RMS}$ is described by the VMRS of the rest measurement. The Signal$_{eff}$ represents the part of the total signal (Signal$_{tot}$) that is different to noise. The total signal is the output signal measured by the DAQ hardware. In all tests conducted according to the protocol, noise was defined as the RMS value of the 5-second rest period measurement. The SNR served as the primary metric for evaluating performance in the single-subject circuit validation. Additionally, the raw EMG signals from the four outputs of the SD6EL circuit were examined, with emphasis on the propagation of the signal.

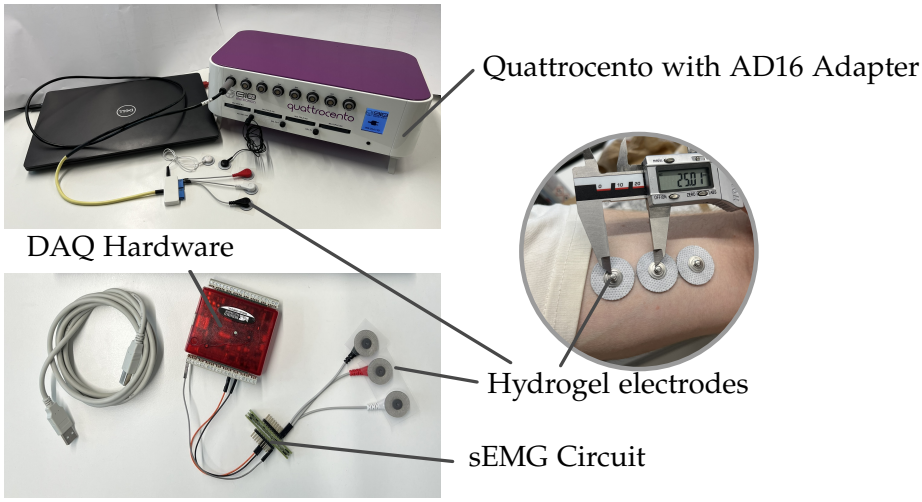

Figure 4.12: Test Setup for comparison between Quattrocento and designed circuits on test person.

Electrodes

Of the three designed PCBs, the 3EL (Figure 4.13 (a)) and 6EL (Figure 4.13 (b)) were tested against the established hydrogel electrodes using the Quattrocento as sEMG hardware. The 4EL PCB shares the same properties, IED, electrode size, and material, as the 3EL, and therefore does not provide additional features that can be tested. To link the electrodes to the Quattrocento adapter AD16 (Figure 4.13 (c)), unshielded cables were soldered directly onto the electrodes of the 3EL and 6EL PCBs. The ground electrode was soldered to a connector compatible with the reference input of the AD16. Measurements were conducted following the isometric contraction protocol described in Section 4.2. Besides the SNR, the impact on the frequency spectrum served as a

secondary criterion for the evaluation of the results. For all measurements following the test protocol, FFT parameter were calculated using the "fft()" function of MATLAB and squared to acquire the power density spectrum (PDS). Mean frequencies were calculated using the following equation:

$$f_{\text{mean}} = \frac{\sum_{k=1}^{N} f_k P(f_k)}{\sum_{k=1}^{N} P(f_k)} \tag{4.3}$$

In this context, f_k is the k-th discrete frequency component obtained from the power spectral density analysis. $P(f_k)$ represents the power spectral density value at frequency f_k, and N is the total number of frequency bins considered in the power spectral density calculation. For evaluation of the frequency spectrum, a digital notch filter at 50 Hz was applied during post-processing to reduce PLI.

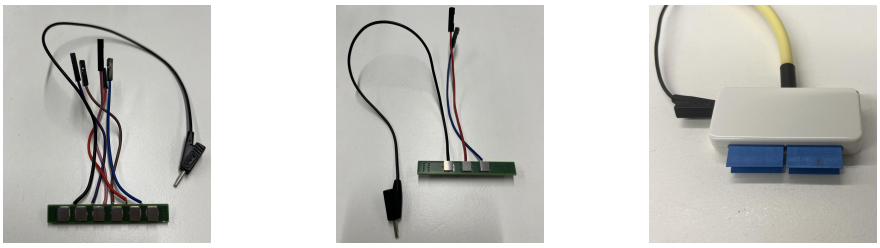

(a) **(b)** **(c)**

Figure 4.13: Electrodes 6EL **(a)** and 3EL **(b)** with cables to connect to the AD16 **(c)**.

4.4 sEMG Sensor Module

The sEMG sensor module consists of the designed electrode connected to the analog circuitry (Figure 4.9). The validation process involved comparing the sEMG sensor module with hydrogel electrodes connected to the Quattrocento, as in the validation of the circuitry (Figure 4.12). Tests were carried out according to test protocol (Section 4.2) used in the validation of the circuits and involved the SD3EL, DD4EL, and SD6EL circuits, all connected to the RedLab 1208FS-PLUS (Meilhaus Electronic, Alling, Germany). The Meilhaus device digitized the analog outputs from the circuits at a sample rate of 2000 samples per second with a 12-bit resolution. This validation assessed the performance of the combined sensor modules, each consisting of designed circuits and electrodes, which were previously validated individually in section 4.3. Testing was conducted on a single subject. Parameters analyzed included power density spectrum, raw sEMG signals ,and mean frequency, with special focus on the transfer

functions effect among the designed circuits. Results of the SD6EL were also tested for propagating MUAPs.

4.5 Wristband Module Validation

To complete the scope of the thesis, the sEMG sensor module (Figure 4.9) is connected to the existing data acquisition module of the DLR research wristband to integrate the sensor module into the wristband (Figure 4.15). Validation of the sEMG wristband module involves testing the wristband modules SD3EL and DD4EL in a user study.

The sEMG signal present at the electrodes is sent through different stages including the amplification stage, filter and bias, which is happening in the analog circuitry described in section 4.3.2 before reaching the DAQ module where the analog signal is converted to a digital signal with a resolution of 12-bit and a 0-3.3 V range. The digital signals are recieved by the microcontroller within the DAQ module and sent to a microcontroller at the master module where it gets transmitted via bluetooth to a computer Figure 4.14. One master module can collect data from multiple sEMG modules as well as other sensor modalities. The electrodes, amplification, and filter circuits are described in section 4.3.2. Next to the microcontroller and ADC, the DAQ module includes a low-dropout regulator to power the IA, operational amplifiers, and voltage converter.

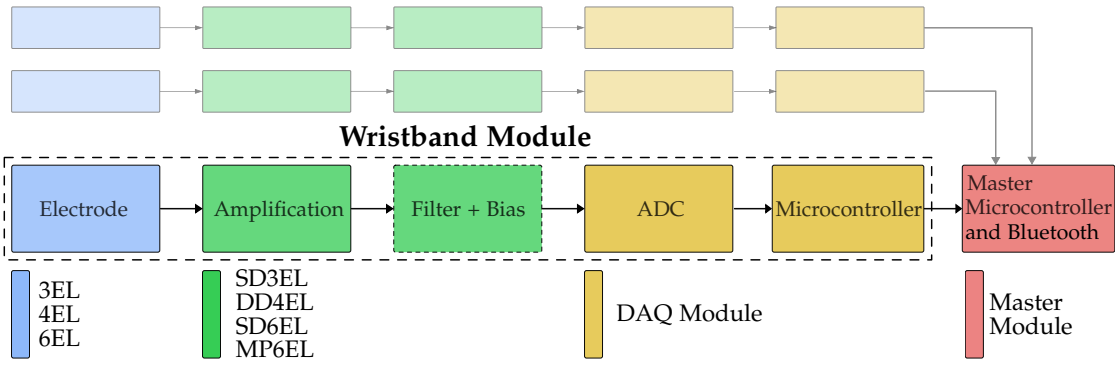

Figure 4.14: Path of the sEMG signal measured with the research wristband. The master module collects data from multiple wristband modules.

The wristband modules were tested by modifying the existing ADC sampling code. This code was adjusted to read the first ADC output containing the sEMG data and transmit it to the master module via serial peripheral interface (SPI) protocol. The 12-bit sEMG data from the ADC is converted to 8-bit data to send via SPI to the master module. The master module transmits the data to a laptop via Bluetooth. The data is

stored with MATLAB using a virtual communication (COM) port. Due to bandwidth limitations, the maximum sampling frequency was limited to 1100 Hz. This frequency meets the Nyquist criterion, but program changes are needed to support multiple wristband modules or record multiple outputs. Bluetooth transmission and a power bank allowed operation without connection to the power grid.

The wristband module contains a stack of PCBs for the electrode, analog circuit, and DAQ inside a housing that matches the length and width of existing modules (see Figure 4.15). To fit the additional PCB, the housing height was increased by 5 mm. A fastening mechanism with a string and a piece of neoprene fabric was added to enable one-handed fastening and to secure the wristband comfortably.

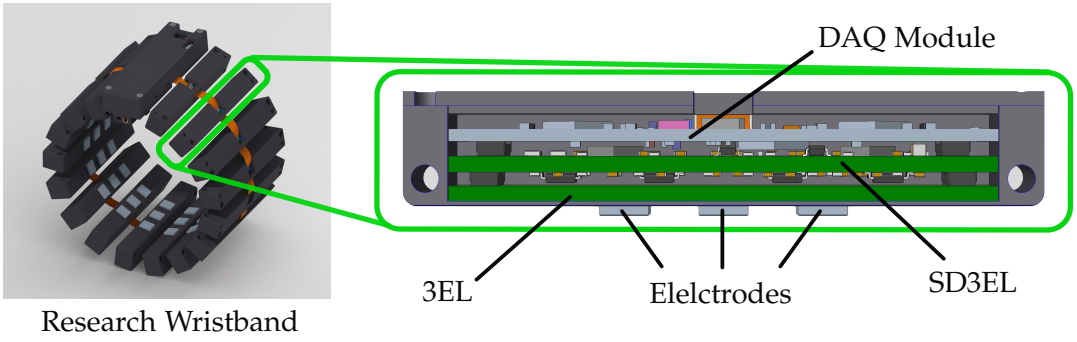

Figure 4.15: Redering of Research Wristband and section view of the wristband module SD3EL.

Two wristband modules, SD3EL and DD4EL, were tested. The user study involved six subjects who each wore the wristband secured to their comfort. Each subject followed the test protocol (section 4.2) for both configuration. During the study, subjects chose their own maximum load rather than strictly following the protocol's 6 kg limit. To avoid interference with electrode contact caused by module movement, a power bank was placed below the arm with no tension on the cable (see Figure 4.16). The user study data was anonymized and randomized to protect participant privacy.

The user study measurements demonstrated a significant reduction in susceptibility to PLI, making the use of a notch filter unnecessary. The study analyzed parameters such as SNR and mean frequency across sensor configurations and subjects.

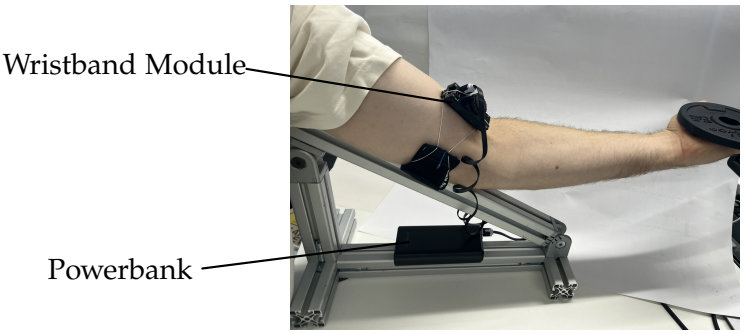

Figure 4.16: Subject of the wristband module user study positioned according to the test protocol.

5 Results

This chapter presents the results of the simulations and validations performed on the designed sEMG circuits and electrodes. The following sections detail the simulation of frequency responses, gain, CMRR, and ADC resolution. Subsequently, validations of the sensor modules and wristband modules are presented.

5.1 Simulation

5.1.1 Frequency Response

Figure 5.1 presents normalized and smoothed FFTs of input and output signals for each of the 4 simulated circuits . The simulated transfer function is obtained of the respective output and input FFTs. The simulated transfer function is compared to an analytic transfer function, which is based on IED, CV, and frequency response of the filter. The coefficient of determination (R^2) between the simulated and analytical transfer function is reported for the frequency range of 20-500 Hz, representing the proportion of variance in the simulated FFT explained by the analytical model within the muscle activity relevant spectrum.

For the MP6EL circuit, the analytic transfer function corresponds to the frequency response of the Sallen-Key band-pass filter (see section 4.1.1). For SD3EL and SD6EL, the analytical transfer function combined the frequency responses of both the band-pass filter and the differential amplifier stage (Figure 2.9). The DD4EL circuit's analytical transfer function is modeled as the square of the SD stage transfer function, multiplied by the filter transfer function. Among all circuits, DD4EL shows the highest correlation with the simulation, with an R^2 of 0.93, indicating that 93 % of the variance in the simulation results is explained by the analytical model. Followed by the two SD circuits with R^2 of 0.92 (SD6EL) and 0.86 (SD3EL). For the MP6EL circuit, the R^2 is the lowest with 0.75.

All transfer functions were normalized to enable comparison between circuits with different A_{AMP} characteristics.

The analysis of mean frequency shifts reveals that SD3EL and SD6EL measure mean frequencies 5.6 % higher than that of the original simulated muscle signal. The DD4EL circuit results in a mean frequency increase of 8.2 % relative to the muscle signal. In

contrast, the MP6EL circuit does not show a significant increase in mean frequency, with values remaining with 1 % of the input.

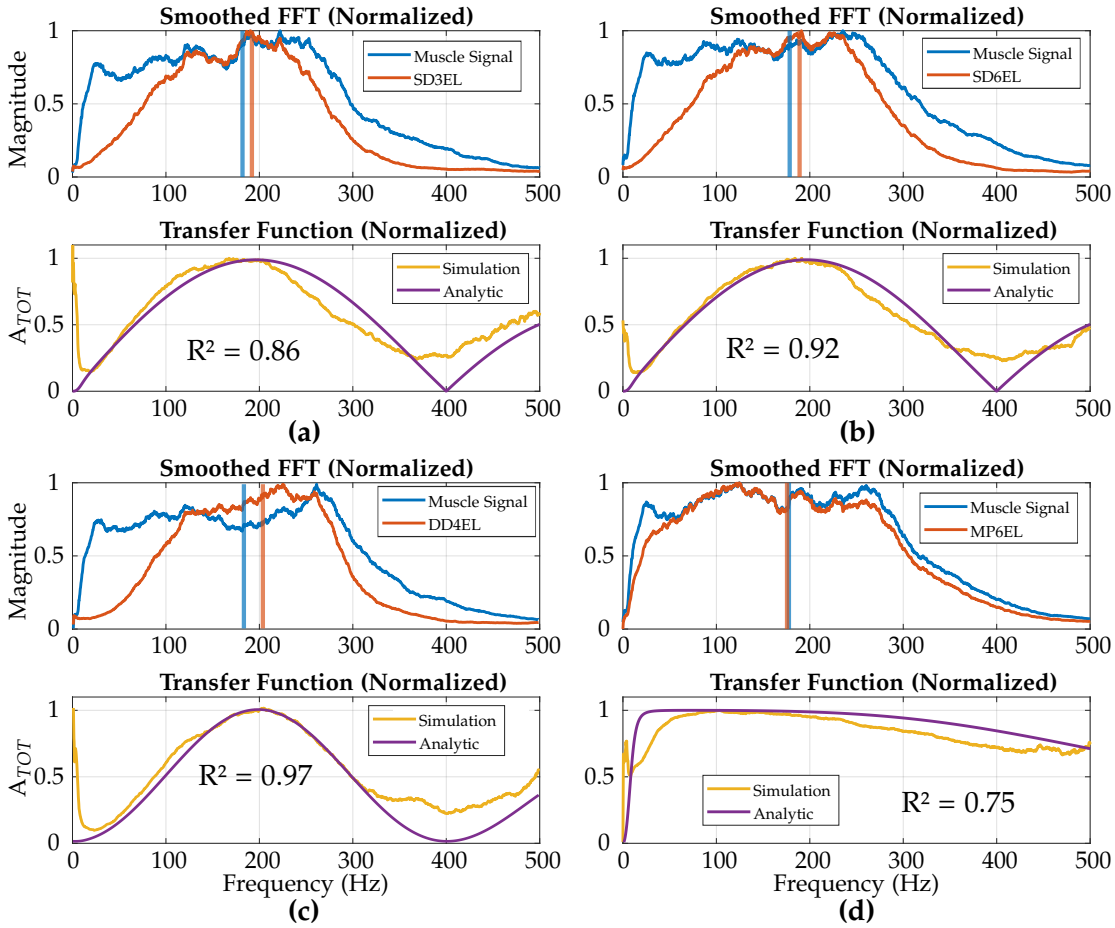

Figure 5.1: Normalized FFT of input and output signals of simulated sEMG circuits with transfer functions based on analytic calculations and simulation results. Mean frequencies are represented by vertical lines. R^2 represents the coefficient of determination between the analytic and simulated transfer functions in the frequency range from 20-500 Hz. FFTs are smoothed with a moving average filter with a width of 100 samples, while simulation results have a resolution of 10 ksamples/second. A simulated muscle signal is used as input. Simulation transfer functions are the amplification factor between the normalized and smoothed circuit output FFT and the normalized and smoothed FFT of the simulated muscle signal. **(a)** SD3EL circuit, **(b)** SD6EL circuit, **(c)** DD4EL circuit, **(d)** MP6EL circuit.

5.1.2 Gain and CMRR

Figure 5.2 displays the calculated values for gain and CMRR across 4 simulated circuits, comparing both ideal conditions (CMRR 0 %$\Delta\Omega$) and the presence of a 10 %$\Delta\Omega$ skin-electrode impedance imbalance (CMRR 10 %$\Delta\Omega$). SD6EL is divided into the first/last and middle outputs because they show a difference of 43 % for the CMRR with 0 %$\Delta\Omega$ impedance imbalance. The first and last output of the SD6EL is corresponding to to outputs 1 and 3 in Figure 2.7 and the middle ones to output 2. The four outputs of the MP6EL showed no significant difference in terms of CMRR and gain, therefore only one output is shown. The A_{TOT} values, represented on the left y-axis, ranged from 216 to 342 and were highest for the SD6EL circuit (339-342), followed closely by SD3EL (329) and DD4EL (295). The MP6EL circuit shows the lowest total gain (216). For the simulation the A_{EL} is equal to 1 because no electrodes sizes are simulated. On the right y-axis, CMRR values spanned from 74 dB to 117 dB. Under equal electrode-skin impedance, the SD3EL and output 2&3 of SD6EL show the highest CMRR with 117 dB and 116 dB respectively, which are dropping 25 and 23 dB to 92 and 93 dB with an increase in skin-electrode impedance of 10 %. With a decrease of from 110 dB to 100 dB under the 10 % imbalance, the MP6EL circuit shows the highest CMRR for for a non ideal conditions. For DD4EL and outputs 1&4 of SD6EL, CMRR values are 75 dB and 81 dB respectively under equal impedance conditions, decreasing lesser than other circuits to 74 dB and 75 dB with the impedance increase.

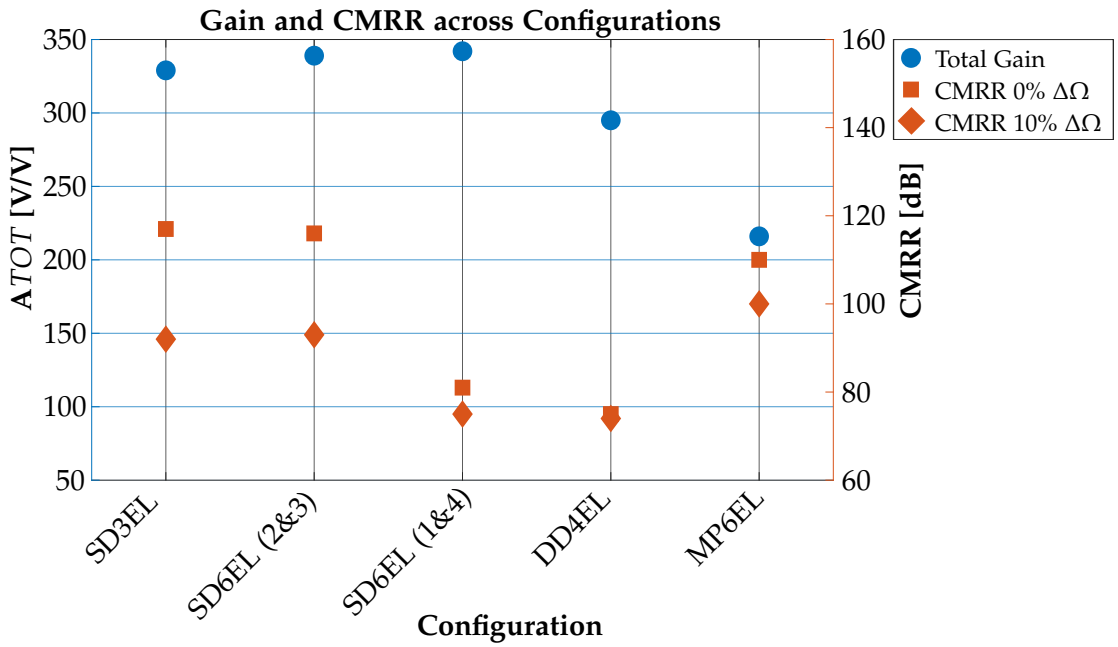

Figure 5.2: Total gain and CMRR across configurations. CMRR are simulated for 0 %ΔΩ and 10 %ΔΩ imbalance in the skin-electrode impedance. SD6EL is divided into first/last and middle outputs.

5.1.3 Analog Digital Converter Resolution

The Resolution of ADC is a critical design consideration for a SEMG sensor system. The ADC must be capable of reliably distinguishing the smallest signal of interest from the inherent noise present at the electrode-skin interface. The ADC (MAX11137) used in the system operates over a 0-3.3V input range and provides 12-bit resolution. The least significant bit (LSB) at the ADC input is therefore:

$$LBS_{ADC} = \frac{3.3V}{2^{12} - 1} \approx 0.81mV$$

Assuming $A_{TOT} = A_{AMP} = 248$, the input-referred LSB (the smallest detectable voltage at the electrode input) is:

$$LSB_{input} = \frac{0.81mV}{248} \approx 3.25\mu V$$

The simulation shows, the baseline noise has a RMS value of 0.01 mV at the inputs and 2.19 mV after amplification and filtering.

5.2 Circuit Validation

Compared to the simulation, common-mode is unknown for real-world tests, thus SNR becomes the primary performance criteria. As second criteria, the total gain of the circuits of acquired for different frequencies is evaluated.

5.2.1 Gain and SNR with Generated Inputs

The top part of Figure 5.3 displays the SNR of the SD3EL, SD6EL, and DD4EL circuits in comparison to the SNR of the Quattrocento system (OTB) across three different frequencies and amplitudes. The SD3EL and SD6EL circuits show SNR differences of less than 2 dB across all tested frequencies and amplitudes, except for a 3 dB difference at 70 Hz and 5 mV. These two circuits deliver equivalent SNRs to the Quattrocento at 170 Hz and 10 mV and at 30 Hz and 2 mV, or surpass it, with only one exception: at 170 Hz and 5 mV, the Quattrocento achieves a SNR of 16 dB, which is 1 dB higher than the SD3EL under the same conditions. The DD4EL circuit consistently shows lower SNR than the Quattrocento - except at 70 Hz and 5 mV - with differences ranging from 0.2 dB at 170 Hz and 2 mV to 4 dB at 170 Hz and 10 mV. The lower plot of Figure 5.3 presents the total gain (A_{TOT}) of the SD3EL, SD6EL, and DD4EL circuits across three different frequencies and amplitudes using generated input signals. For the generated input tests, both A_{EL} and A_{DIFF} are equal to 1 because the signal is non-differential and electrodes are not employed. The SD3EL and SD6EL circuits show nearly identical gain at fixed frequency conditions, with values ranging from 133 to 140 at 30 Hz across amplitudes to a peak of 260 at 170 Hz and 2 mV (SD3EL). The difference between the two circuits does not exceed 10 V/V at any data point. In contrast, the DD4EL circuit consistently shows lower A_{TOT} across all frequencies and amplitudes, with values ranging from 92 V/V at 30 Hz and 10 mV to a maximum of 128 V/V at 170 Hz and 2 mV.

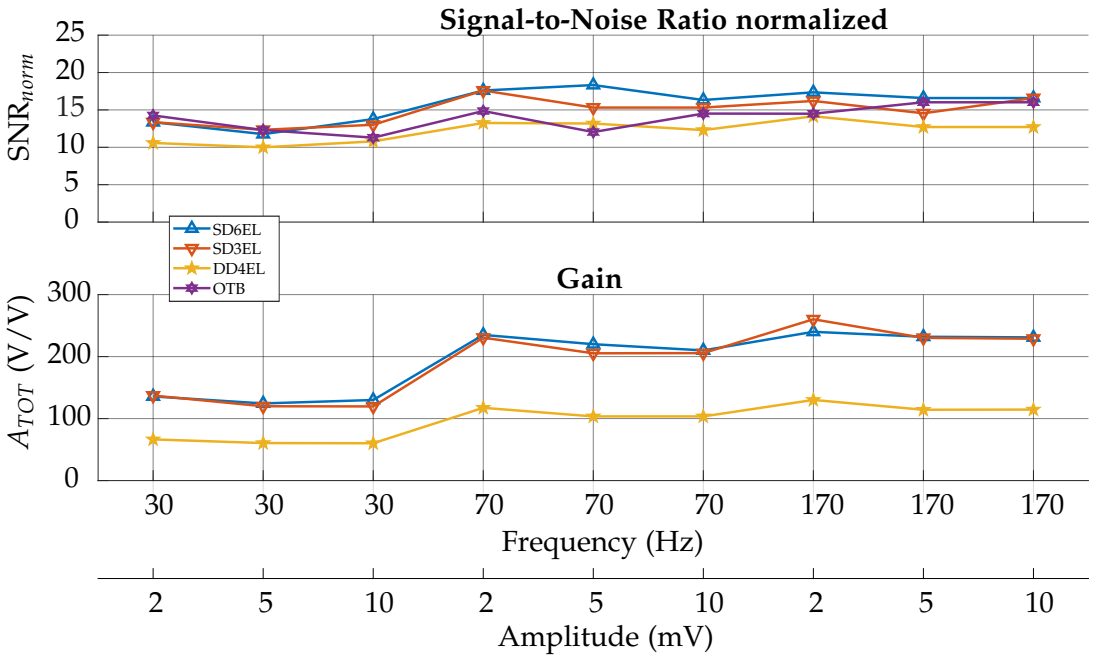

Figure 5.3: Top: SNR comparison of designed circuits and OTBioelettronica Quattrocento with generated inputs across three different frequencies and amplitudes. Bottom: Total gain of designed circuits across three different frequencies and amplitudes.

5.2.2 SNR and Raw Signal of sEMG of Upper Arm

The SNR results for the single-subject study for the circuit validation using hydrogel electrodes are depicted in Figure 5.4. Circuit SD6EL is divided into four outputs, corresponding to the five differential electrodes of the circuit. The SD3EL circuit shows SNR values that are 2.5 dB higher than those of the Quattrocento for loads of 1 and 2 kg. For higher loads, the Quattrocento achieves SNRs between 0.5 dB and 3 dB greater than those of the SD3EL. SD6EL outputs 1 and 4 show equal results for loads above 2 kg, and a difference of 1.5 dB at 1 and 2 kg, where SD6EL (1) shows higher values. Output 2 of SD6EL consistently shows SNR values 2 dB lower than SD6EL (4) across all load levels. The DD4EL circuit presents SNR values below 0.5 dB difference to the Quattrocento at 1,2 and 3 kg loads, while showing decreases of 3.5 dB at 4 and 6 kg, and 6 dB at 5 kg. Output 3 of SD6EL shows notably lower SNR values than the other circuits across all loads, with differences from the Quattrocento ranging from 5 dB at 5 kg to 13 dB at 6 kg.

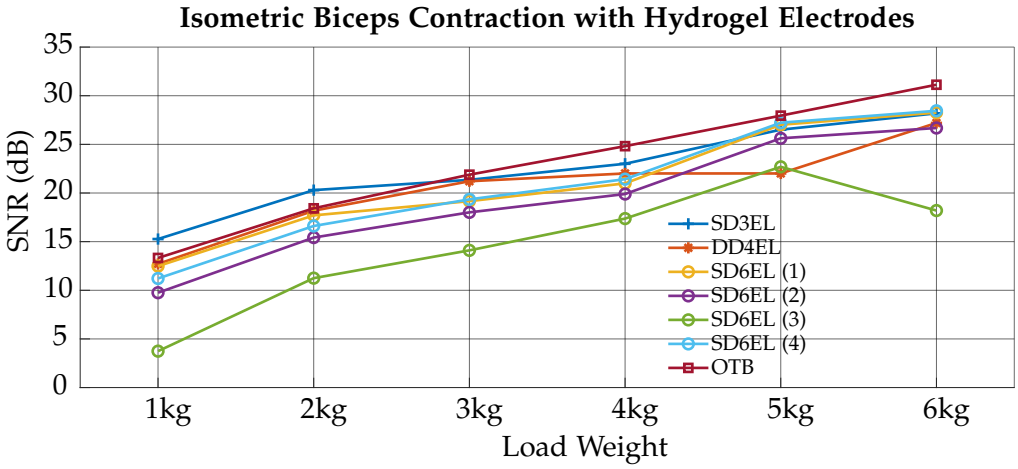

Figure 5.4: SNR of designed circuits and OTB Quattrocento system for an isometric biceps contraction across different loads applied over 5 seconds and measured with hydrogel electrodes.

During the validation of the SD6EL circuit, electrodes in the six electrode configuration were spreading across the majority of the biceps due to the size of the electrodes (Figure 5.8 (c)). Figure 5.8 (a) shows the raw sEMG signal of the four outputs from the SD6EL circuit for an isometric biceps contraction while a 6 kg load is applied to the hand. The signals are plotted over a time window of 0.45 seconds to increase visibility of the individual signal peaks. Outputs 1, 2 and 4 show peaks in a time frame of 0.02 s. Output 2 and the inverted signal of output 4 is shown in Figure 2.3 (b). Signal 4 is inverted by multiplying the magnitude by -1. The two signals show a coefficient of determination (R^2) of 82 %.

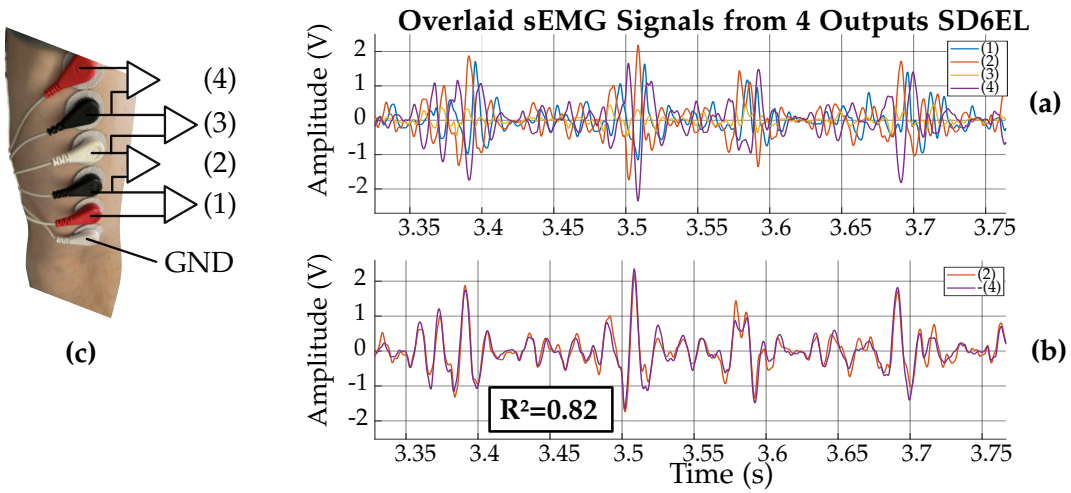

Figure 5.5: Raw sEMG signal of SD6EL circuit with 6 hydrogel electrodes. Isometric biceps contraction with 6 kg weight load. **(a)**: 4 outputs of SD6EL overlaid for a time frame of 0.45 seconds. **(b)**: Output 2 and inverted signal of (4) by multiplying its amplitude by -1. **(c)**: applied hydrogel electrodes on biceps.

5.3 Electrode Validation

Electrodes, alongside the circuit, are another major factor in reducing PLI. SNRs of configuration employing the 3EL, 6EL, and hydrogel (OTB) electrodes are displayed in Figure 5.6 to evaluate the effect of the electrode on the PLI. SNR acquired using the 6EL is divided into the 4 differential outputs corresponding to the electrode. Figure 5.6 shows the SNR for the tested electrodes across different weight loads with no further filtering in the post-processing and with an digital 50 Hz notch filter applied. Values of the designed electrodes show lower SNRs compared to the hydrogel electrodes regardless of the filters used. Differences range from 11 dB for the 6EL (2) at 6 kg without filtering to 48 dB for the 6EL (3) at 2 kg without notch filter. Without filtering, SNR values of the electrodes 3EL at 1 kg and SD6EL outputs 1, 3, and 4 for loads below 5 kg are negative. This corresponds to root mean square voltage (VRMS) noise being higher than the VRMS of the muscle signal. The designed circuits achieve SNR values of at least 6 dB with 50 Hz notch filtering, and the SNR increases markedly with the load weight.

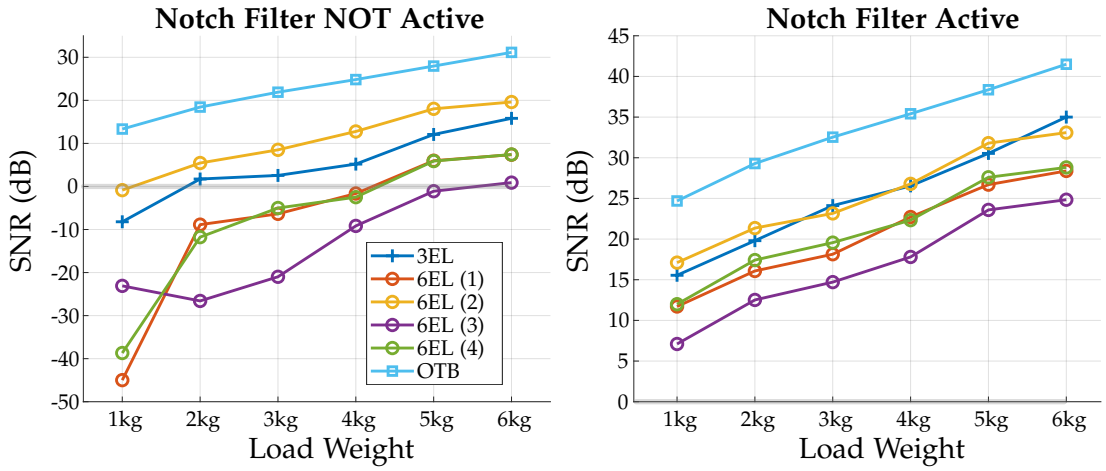

Figure 5.6: SNR for configurations using the 3EL and 6EL electrode designs, as well as hydrogel electrodes (OTB), across different weight loads for a 5-second isometric biceps contraction. For the 6EL, SNR is shown separately for each of the four differential outputs. The left graph presents SNR values without additional digital filtering in post-processing, while the right panel shows SNR with a digital 50 Hz notch filter applied.

As highlighted in the literature, properties of electrodes used in sEMG have a significant influence on the frequency spectrum of the recorded signal [44]. Figure 5.7 displays the mean frequency across measurements with different electrodes versus the weight load. The results for the designed steel electrodes with a contact are of 5 x 6 mm are illustrated in a boxplot, which displays the distribution, median, minimum, and maximum value of mean frequencies. The boxplots comprise the mean frequencies of the four 6EL and the 3EL signal. Without filtering, variability (size of the box) is decreasing with increasing load weight, with 4 kg being an exception. Similarly, the median of the mean frequency is increasing with load. This cannot be seen with a notch filter active. With filtering, mean frequencies of the designed steel electrodes are significantly higher than frequencies of configuration using hydrogel electrodes. Differences range from 40 Hz at 5 kg to 59 Hz at 1 kg. The diameter of the hydrogel electrode is 24 mm.

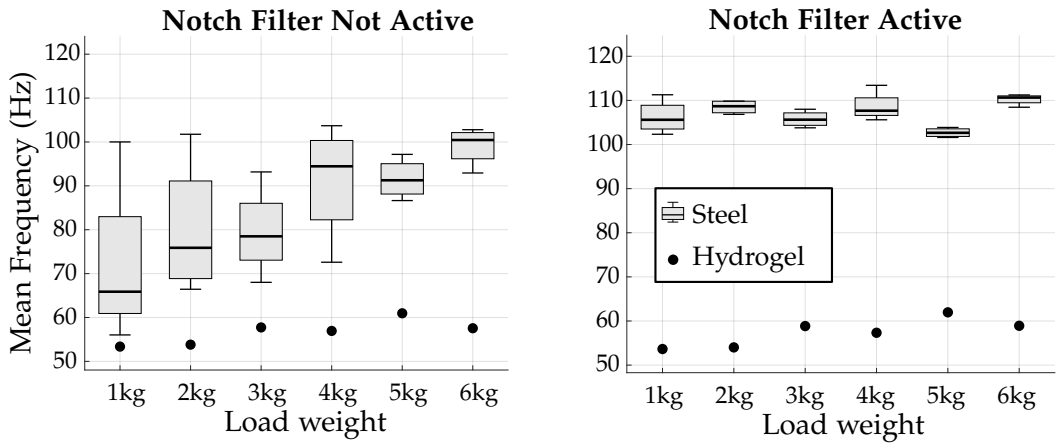

Figure 5.7: Mean Frequencies of steel electrodes (3EL & 6EL) compared to hydrogel electrodes across different weight loads. Data was collected over 5-second isometric biceps contraction. The results are shown without filtering and with an active 50 Hz notch filter. Hydrogel electrodes provide effective active grounding of the patient, which results in the notch filter having no significant impact on the mean frequency.

5.4 Sensor Module Validation

The measurements with the SD6EL circuit and the 6EL electrode yielded clear raw sEMG signals during a five-second isometric biceps contraction for both loading conditions. The top plot in Figure 5.8 shows sEMG responses under a 3 kg load, while the bottom plot displays signals at 6 kg. The four outputs of the SD6EL circuit are shown over a 0.16-second time window, with a digital 50 Hz notch filter applied. The electrodes corresponding to output 1 are positioned closest to the muscle center, while the electrodes linked to output 4 are the farthest. For both load conditions, the time interval between signal peaks from consecutive outputs ranges between 0.0015 and 0.0025 seconds. The minimum time step, defined by the 1100 Hz sampling rate, is 0.0005 seconds. Signal amplitudes increase notably under the 6 kg load with peaks showing a maximum absolute value of 0.15 V and 1.51 V for 3 kg and 6 kg respectively.

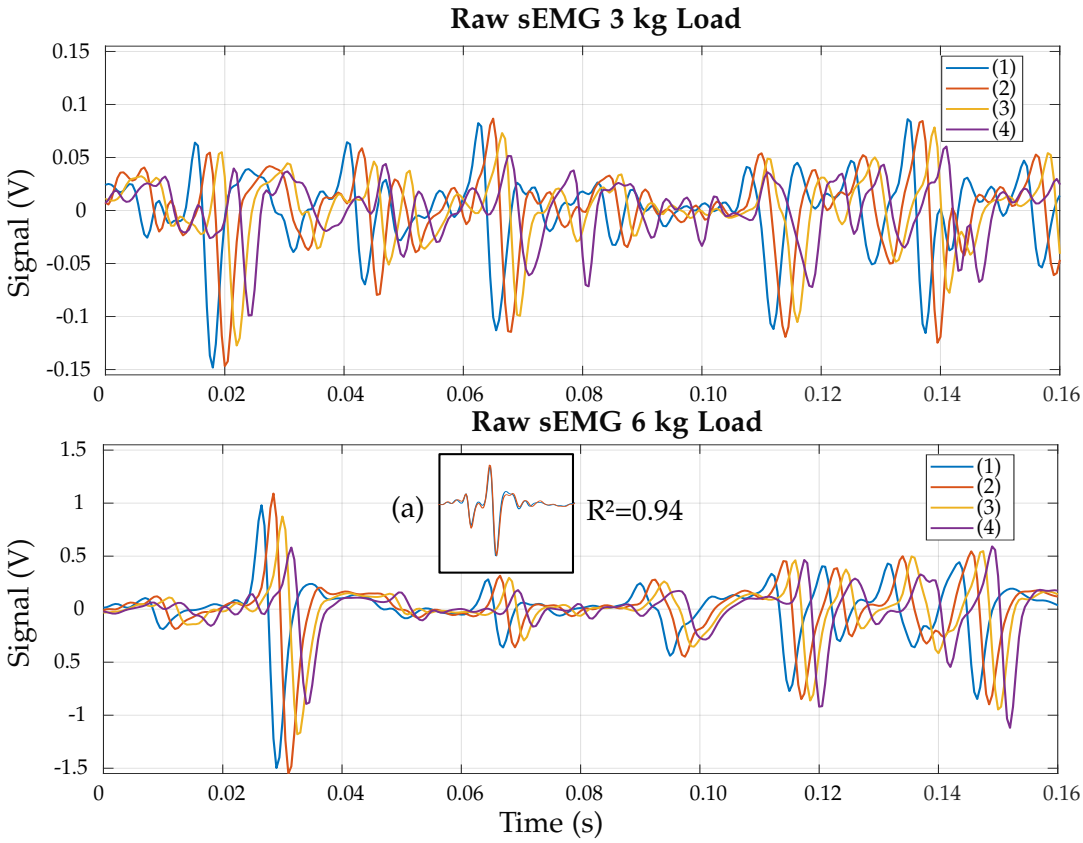

Figure 5.8: Raw sEMG signal over 0.16 second time window for 3 kg load (top) and 6 kg (bottom). (a) shows an overlay of output 1 delayed by 0.002 s and output 2, which results in a coefficient of determination of 94 %. Measured with SD6EL in combination with electrode 6EL over a 5 second isometric biceps contraction with a 1100 Hz sample rate. A digital 50 Hz notch filter was applied to the signals.

Figure 5.9 displays the PDS of the SD3EL sensor module alongside the Quattrocento setup with hydrogel electrodes for three different loads (1 kg, 3 kg, and 6 kg). To improve visibility, the PDS was smoothed using a moving average filter of size 50. The power density spectrum shows how signal power distributes across frequency components, quantifying the energy at each frequency to highlight the dominant frequencies produced by muscle activity and motor unit action potentials.

The OTB system exhibits higher PDS values than the sensor module in the frequency range from 1 to 70 Hz, with this difference becoming more pronounced at higher loads.

The smoothed PDS curves for the OTB system decrease approximately linearly from 50 Hz to 160 Hz, dropping to levels below 0.005 $V^2\,Hz^{-1}$.

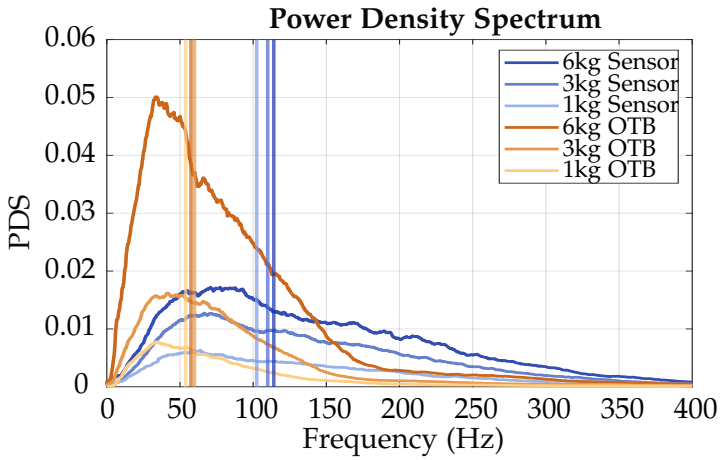

Figure 5.9: Power density spectrum and mean frequencies of SD3EL sensor module and reference system across three different loads for an isometric biceps contraction. The data was smoothed using a moving average filter with a width of 50 samples and a 50 Hz digital notch filter was applied.

Figure 5.10 presents the mean frequencies of the sensor modules alongside the reference system. The reference system employs hydrogel electrodes with a diameter of 24 mm, which restricts the minimum (IED) to 25 mm. In contrast, the sensor modules use six electrodes each measuring 5 mm in length along the muscle fiber direction. The IED is 10 mm for both the SD3EL and DD4EL modules, and 8 mm for the SD6EL module. Each sensor measured an 5 second isometric biceps contraction for loads from 1 to 6 kg.

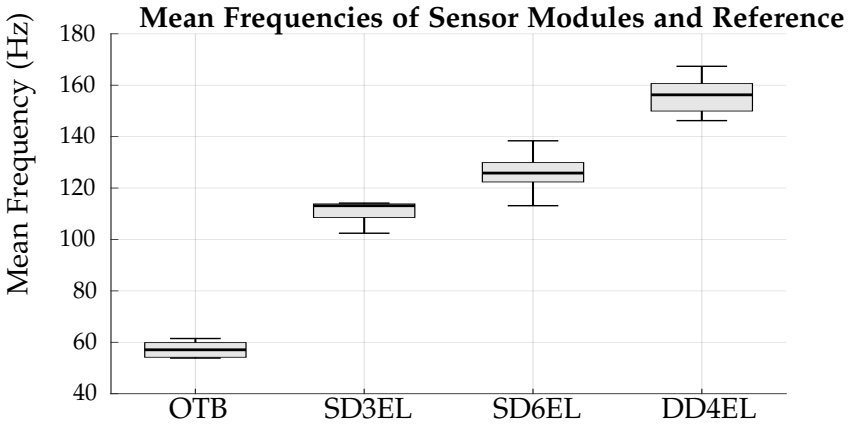

Figure 5.10: Mean frequencies of sensor modules, SD3EL (10 mm IED), SD6EL (8 mm IED), DD4EL (10 mm IED), and reference system (25 mm IED) for an isometric biceps contraction. The sample rate was set to 2000 Hz. Each sensor measured six different loads. A 50 Hz notch filter was applied to the data before calculating the mean frequencies.

5.5 Wristband Module Validation

SNR results for both wristband sensor modules, SD3EL and DD4EL, are presented across a range of weight loads from 1 kg to 8 kg for six subjects (Figure 5.11). Each line in the plots corresponds to an individual subject, illustrating variation in SNR performance. The SD3EL module shows a higher SNR overall, with several subjects achieving values above 30 dB at increased load weights, while the DD4EL module show lower SNRs, with values remaining below 30 dB for all subjects. For both modules, SNR tends to improve as the load weight increases. SNR presents significant variability between subjects, with differences reaching up to 25 dB between S2 and S6 at a load of 3 kg.

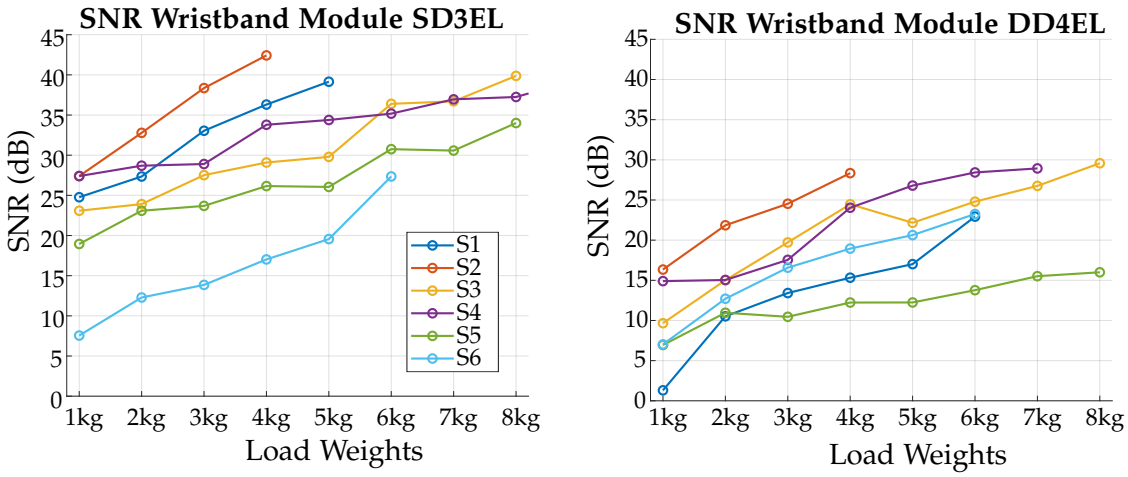

Figure 5.11: SNR of the wristband modules SD3EL and DD4EL across different weight loads for six subjects. A notch filter was not applied due to reduced PLI during battery-powered operation. Data was sampled at a rate of 1100 samples/second.

Figure 5.12 shows box plots of mean frequency measurements for the SD3EL and DD4EL wristband sensor modules across the six subjects. Across all subjects, the DD4EL module consistently presents higher mean frequencies than the SD3EL module. While both modules show inter-subject variability, the difference in mean frequency between modules is most pronounced for subjects S3 through S5, where DD4EL values reach above 130 Hz and SD3EL values remain closer to or below 120 Hz.

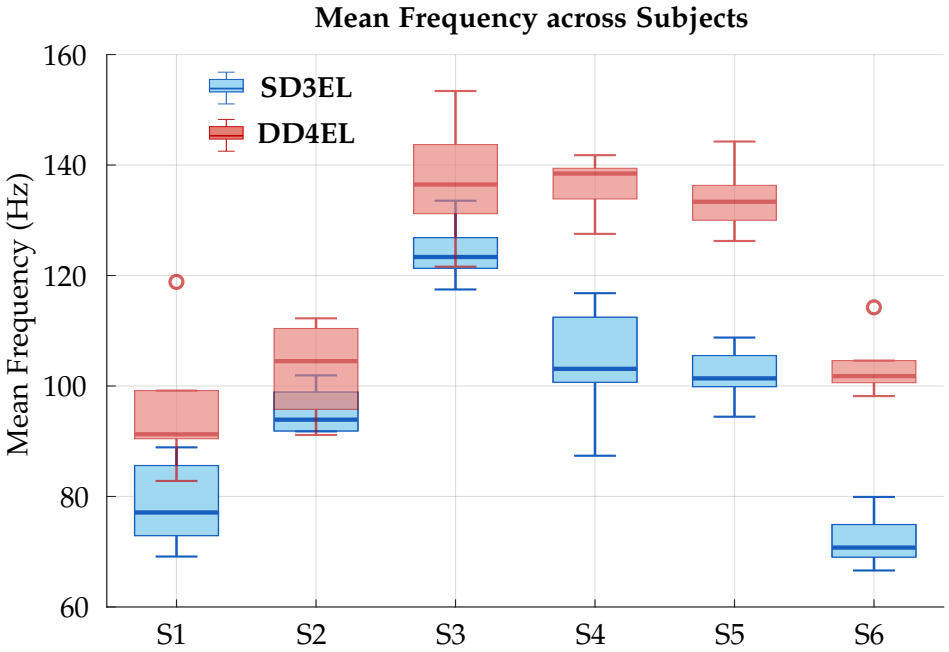

Figure 5.12: Box plots of mean frequencies of SD3EL and DD4EL wristband modules across six subjects. The mean frequency calulated across all loads measured for each subject (Figure 5.11) without notch filter.

6 Discussion

6.1 Simulation

6.1.1 Frequency Response

The influence of the spatial frequency response for all circuits is evident in the FFTs, with correlations ranging from 75 % (MP6EL) to 97 % within the relevant frequency spectrum (20-500 Hz). The calculated transfer function - based on a given IED, CV and electrode size - explain significant proportions of variance (86 % for SD3EL, 92 % for SD6EL, 97 % for DD4EL, and 75 % for MP6EL). Consequently, these transfer functions can be employed in post-processing to more accurately represent the input frequency spectrum within the amplified output signal of the simulation.

The simulation results emphasize that the transfer function should be considered when evaluating SD circuits in practical applications. For instance, if the mean frequency of a voluntary contraction increases from 100 to 130 Hz, the RMS of the SD output signal increases more strongly than the muscle signal is indicating. This occurs because frequencies between 130 and 200Hz are amplified more intensely than those between 100 and 130 Hz (Figure 5.1 (a)).

For the DD4EL circuit, the spatial transfer function is squared because of the second amplification stage (Figure 5.1 (c)). Frequencies below 100 Hz and above 300 Hz experience >40 % less amplification compared to signals centered at 200 Hz. At the boundaries of the sEMG spectrum (10-30 Hz and 400-500 Hz), this attenuation is even more pronounced, reaching 60-80 % less total gain. These results indicate that without appropriate post-processing to compensate for frequency-dependent gain, DD based sensors provide less accurate representation of the true frequency content of muscle signals.

Furthermore, simulations demonstrate that the SD3EL and SD6EL circuits overestimate the mean frequency of the output signal by 5.6 %. This arises because their transfer function peak at higher frequencies (200 Hz) relative to the muscle signal's mean frequency (167 Hz), effectively shifting the differential output towards the transfer function's peak. In the DD4EL circuit, this overestimation increases to 8.2 % due to the second differential stage. Collectively, the results highlight a limitation in the ability of differential based sensors to accurately represent muscle signals, particularly when

frequency characteristics are of interest.

6.1.2 Gain and CMRR

This section discusses the results of the total gain and CMRR characteristics of the evaluated circuits, with emphasis on their implications for electromyographic signal quality and robustness.

The total gain of the circuits depend on the frequency spectrum due to the transfer function of the amplification stage as shown in Figure 5.1. The SD circuits show significantly higher A_{TOT} (329-342) compared to the monopolar configurations, despite employing the same amplifier and gain resistors. This increase arises because, for the given IED, CV, and input frequency spectrum, the differential stage amplifies the signal by effectively taking the difference between the same signal delayed by the propagation time between the two electrodes (0.0025s).

For the DD4EL circuit, the gain resistors have double the value of those in the SD amplifiers (R4, R5 in Figure 4.5), reducing the A_{AMP} to half that of the SD amplifiers. This adjustment compensates for the additional gain contributed by the second differential stage's transfer function. Without this gain reduction in the first differential stage, the output of the DD4EL circuit saturates the amplifiers in the simulation. The gain resistors of the DD4EL sensor circuit were specifically designed based on the simulation results.

CMRR represents a key metric for sEMG circuits, directly influencing the SNR and thus the overall sensor performance. The simulation quantifies CMRR degradation due to the voltage divider effect caused by skin-electrode impedance.

A decrease in CMRR due to this imbalance is observed in the SD3EL and SD6EL (2&3) circuits. In both, the same current flows through the electrode-skin impedance connected to the amplifier inputs. For SD3EL, this current corresponds to the amplifier's input bias current. In the SD6EL (2&3) circuit, each electrode connected to the amplifier inputs is tied to two inputs (as shown in Figure 2.7, input B), effectively doubling the current through each electrode-skin impedance. Because the voltage drop across each impedance is proportional to the current, an ideal impedance balance ($0\Delta\Omega$) results in no conversion of common-mode to differential signals, yielding maximal CMRR values of 117 dB (SD3EL) and 116 dB (SD6EL, 2&3). However, a 10% impedance imbalance causes the voltage divider effect to convert common-mode signals into differential signals, which are amplified (see Subsection 2.2.2), leading to respective CMRR reductions of 25 dB and 23 dB for SD3EL and SD6EL (2&3) respectively.

In contrast to the SD3EL and SD6EL (2&3), the DD4EL, SD6EL (1&4), and MP6EL circuits share the characteristic that the electrode-skin impedances connected to the amplifier inputs are connected to varying number inputs. For instance, signal A

is connected to one amplifier whereas signal B connects to two inputs (Figure 2.7). Consequently, current through the electrode-skin impedance differ, one experiencing the input bias current once, the other twice. This current imbalance causes a different voltage drop over the impedances resulting in a conversion of common-mode to differential signal even for an imbalance of 0 $\Delta\Omega$. This causes in CMRR degradation and explains the lower CMRR of 75 dB and 81 dB for DD4EL and SD6EL (1&4) respectively.

This effect is multiplied in the MP6EL configuration, where the reference electrode feeds into four inputs resulting in current four times the input bias current. To prevent this significant CMRR degradation, input buffers serve as impedance converters before amplifier inputs, improving robustness against impedance imbalances. This buffer stage enables the MP6EL circuit to achieve an CMRR of 110 dB for ideal conditions and 100 dB for 10 % imbalance. buffer stage is making the Circuit more robust against impedance imbalances.

6.1.3 Analog Digital Converter Resolution

The ADC resolution is a critical design consideration for a SEMG sensor system. The ADC must be capable of reliably distinguishing the smallest signal of interest from the inherent noise present at the electrode-skin interface.

The dominant noise source in sEMG acquisition arises from the electrode-skin interface. As reported by Huigen et al. (2002), wet electrodes introduces noise levels up to 10 μV [85]. However, with dry electrodes, the impedance at the interface increases, leading to higher noise up to 150 μV depending on the size, material and skin preparation [86]. Since the designed system includes dry stainless steel electrodes on unprepared skin, the higher noise figure is the relevant limiting factor for system sensitivity. The simulation showed that the ADC resolution of 12 bits corresponds to a LSB of 3.25 μV at the inputs of the circuit, which is significantly smaller than the expected noise of 10 μV. Based on the values found in the literature, this value is on the lower than the expected noise level. Therefore, the ADC provides a sufficient resolution to detect electromyographic signals using dry electrodes.

6.2 Circuits Validation

This section discusses the validation of the designed sEMG circuits using both generated inputs and real upper arm measurements. It compares SNR and total gain performance across the SD3EL, SD6EL, DD4EL, and a reference system to assess amplification, filtering, and common-mode rejection.

6.2.1 Generated Inputs

SNR of SD3EL and SD6EL values being higher or equal to the Quattrocento indicate that the circuits provide better or equal performance regarding CMRR when dealing with equal inputs (Figure 5.3). Equal values of the SD3EL and SD6EL compared to the lower values of the DD4EL suggests that measurements are consistent because SD3EL and SD6El employ the same amplification and filter stages. Results suggest less performance of the DD4EL in terms of SNR and therefore CMRR compared to SD3EL, SD6EL and the reference system. If this is due to the reduced amplification stage gain (A_{AMP}), CMRR for a DD4EL with increased A_{AMP} should be tested in future investigations.

All designed circuits show total gain variation across frequencies. The circuits amplify 70 Hz and 170 Hz signals stronger than 30 Hz signals. The Sallen-Key high-pass filter's transfer function can explain part of this variation. The DD4EL's reduced A_{TOT} for all frequencies results from the lower A_{AMP} of its first amplification stage. Simulated transfer functions for differential amplification do not affect results with generated inputs, because these inputs use a reference ground instead of true differential signals resulting in A_{DIFF} of 1.

6.2.2 SEMG of Upper Arm

In Figure 5.4 SD6EL output 2 and 4 show the same gradient just level shifted indicating similar signals were recorded at each input but different noise levels. SNR investigations in the single-subject study demonstrated that the SD3EL and SD6EL circuits, when used with hydrogel electrodes, delivered comparable SNR performance. Differences compared to the Quattrocento system ranged between 1 and 5 dB. The size of the electrodes causes the array of electrodes to spread over the complete muscle. Parts of the sensor are therefore above the innervation zone. The missing peaks and lower amplitude of signal (3) in Figure 2.3 (a) indicate that the innervation zone is located below the electrodes linked with output 3. Supporting this, signal (2) and (4) show an inverted relation. Figure 2.3 (b) shows that the negative of signal (4) explains 82 % of the variance of the signal (2), as reflected by the coefficient of determination (R^2) of 82 %. This relationship can be explained by a MUAP propagating in opposite directions along the muscle fiber, being simultaneously detected by both differential channels.

To conclude, the designed sEMG sensor circuits SD3EL and SD6EL demonstrated consistent and comparable SNR performance to the reference system, validating the simulation results for amplification and common-mode rejection. These circuits effectively detect and amplify myographic signals, confirming their suitability for sEMG measurement. While the DD4EL exhibited lower SNR and A_{TOT}, it still detected myographic

signals, indicating its capability despite reduced performance. Gain characteristics are further discussed in section 6.5.

6.3 Electrodes Validation

Figure 5.6 illustrates how the different electrode influence the SNRs of a sEMG system. Steel electrodes show a significantly higher susceptibility to common-mode, interference resulting in reduced SNR. This reduction can be caused by the increased skin-electrode impedance of the steel electrode compared to the sticky electrode. Increased impedance at the grounding electrode lowers the effectiveness of active grounding. Secondly an increase in skin electrode imbalance can further enhance the amplification of common-mode voltage by the sensor. The low impedance at the skin-to-hydrogel interface provides excellent patient grounding. As a result, and because the measured mean frequency is close to 50 Hz, there is no observable difference in mean frequency whether a notch filter is applied or not. Figure 5.6 also shows the effect of PLI using steel electrodes resulting in negative SNRs, while also illustrating how a notch filter at powerline frequency can improve SNR but not reaching the same values as hydrogel electrodes. The lower VRMS of filtered steel electrode signals results from attenuation caused by the increased skin-electrode impedance (see section 2.2.2).

Figure 5.7 show the effect of different electrodes on the mean frequency of the detected sEMG signal. Without filtering, the reduction in variance with increased load is caused by the increased SNR with higher loads (see Figure 5.6). If SNR increases the signal is less dominated by PLI. With the PLI filtered out, the steel electrodes show markedly increased mean frequencies ($\Delta F > 50$ Hz) for equal loads compared to hydrogel electrodes. These finding can be explained by the transfer function of the differential electrodes, with IED of 10 mm for the 3EL and 8 mm for the 6EL. The transfer function causes stronger amplification of signals between 100 and 200 Hz compared to lower frequencies (see Figure 2.9). Another reason for the lower mean frequencies of the hydrogel electrodes is the low pass filtering introduced by the greater size of the electrode. Hydrogel electrodes have a contact area of 425 mm^2 compared to 30 mm^2 for the steel electrodes. This effect is further discussed in section 6.4.

To conclude, in the tested configuration with the Quattrocento, the designed steel electrodes do not provide sufficient SNR without a notch filter applied in post-processing. However, they provide superior low-pass filtering characteristics for sEMG compared to hydrogel electrodes.

6.4 Sensor Module Validation

The raw signal for load 3 kg and 6 kg (Figure 5.8) indicate that the four outputs of the SD6EL sensor module share the same amplitude profile with a delay of 0.002 s to the next output for both loads. The correlation is proven by the coefficient determination of 94 %. This cross-correlation based on the expected CV of 4 m/s and known IED of 8 mm provides quantitative prove of signal propagation between two electrodes.

PDS of the OTB system shows a maximum of a detectable frequency of 170±10 Hz (Figure 5.9). This limit arises from the electrode size. The minimal wavelength an electrode can detect depends on its length along the propagation direction. For the circular electrode, this minimal wavelength is 24 mm, corresponding to a maximum frequency of 166.67 Hz based on a CV of 4 m/s. For the designed electrodes with a length of 5 mm, the maximum detectable frequency is 800 Hz, which exceeds the maximum frequency of interest (500 Hz). This demonstrates the superior ability of the designed electrodes to accurately represent the frequency characteristics of the muscle signal.

The low-pass filtering effect of electrode size is also seen in the mean frequencies of the OTB system across all load conditions (Figure 5.10). Comparing the mean frequencies of steel electrodes connected to the SD3EL (Figure 5.10) with those of steel electrodes using the Quattrocento system (Figure 5.7) reveals comparable results, indicating similar frequency response performance of the analog circuitry when using steel electrodes. Since all designed sensors use electrodes of the same size, differences in mean frequency among the sensor modules arise from variations in transfer functions caused by differential amplification and inter-electrode distance (IED). The SD6EL's 8 mm IED, compared to the SD3EL's 10 mm, shifts the transfer function peak from 200 Hz to 250 Hz. This simulation-predicted shift explains the higher mean frequency observed for the SD6EL relative to the SD3EL. Additionally, the DD4EL shows a higher median mean frequency (156 Hz) compared to the SD6EL (126 Hz) and SD3EL (112 Hz), due to its double differential amplification stage, which amplifies signals between 100 Hz and 200 Hz more strongly than the single differential stages used by the other modules.

In conclusion, the raw signal demonstrates the capability to detect propagating signals. The mean frequency analysis aligns with simulation predictions of the transfer function. When interpreting sEMG data, it is essential to consider both the IED and the acquisition modality. Ignoring the transfer function can result in differing frequency spectrum outcomes when measuring the same muscle activity with different sensor configurations, such as SD and DD modalities. These variations can affect the performance of decomposition algorithms, which rely on consistent signal patterns to accurately identify motor unit action potentials and decode muscle activity.

6.5 Wristband Module Validation

Mean frequencies and SNR variations across subjects reflect the physiological differences between individuals (Figure 5.12). The smaller variance within each subject's mean frequency measurements for both sensors, aside from two outliers, demonstrates consistency in data collection. The sensors' functionality is further indicated by an increase in SNR, and consequently the VRMS of the signal, with higher load weights (Figure 5.11). The complete wristband modules are capable of detecting low frequencies between 40 Hz and 80 Hz (e.g., subjects S1, S6), as well as medium and high frequencies ranging from 80 Hz to 120 Hz (S4, S5) and above 120 Hz (S3). The lower SNR observed in the DD4EL module compared to the SD3EL module can be due to its reduced A_{TOT}, motivating further investigation with increased DD4EL A_{AMP}.

The SD3EL wristband shows SNR values consistently above 20 dB without the application of a notch filter, indicating that power line interference is substantially lower compared to recordings with the Meilhaus device. The improved signal quality results from eliminating the power grid connection, confirming the advantages of battery-powered data acquisition.

Contrary to simulation expectations, the second differential stage does not provide the anticipated gain effect. The DD4EL circuit exhibits significantly less A_{TOT} than the single differential circuits, and the raw DD4EL signals remain well below the amplifier saturation voltage. Simulations guided the A_{AMP} adjustment of the DD4EL to prevent amplifier saturation, as the simulated muscle signals showed peak amplitudes within 20 Hz to 167 Hz. The double differential stage's transfer function, peaking near 200 Hz, strongly amplifies signals at 167 Hz, causing saturation in simulations and leading to the decision to reduce the A_{AMP}. However, real-world signals above 100 Hz are weaker than modeled, resulting in A_{TOT} reduction in practice.

A_{AMP} values were kept sufficiently low to avoid amplifier saturation; the highest output signals reached about 3 V, which corresponds to 91% of the saturation voltage. Therefore, increasing A_{AMP} for the SD6EL and SD3EL modules is unnecessary, but the DD4EL should be tested with increased A_{AMP}. Figure 5.12 supports the hypothesis that double differential acquisition increases the observed mean frequency across multiple subjects.

In conclusion, the results highlight the sensors' ability to consistently measure meaningful muscle signal features across diverse subjects and loading conditions. Additionally, sensor-specific design choices, such as gain settings and differential stages, significantly influence signal quality and frequency characteristics and should be optimized for practical applications.

7 Summary and Outlook

This thesis introduces a customizable sEMG sensor module designed for the DLR research wristband. The modular design integrates interchangeable electrodes and analog signal processing circuits, enabling diverse configurations tailored to various experimental needs in both research and teaching environments.

The work combines detailed circuit simulations with synthetic EMG signal generation to evaluate key electrical parameters such as amplification gain, frequency response, and CMRR. Four different acquisition configurations, monopolar, single differential (3 and 6 electrodes), and double differential, were modeled and analyzed. The simulated transfer functions reveal significant frequency-dependent effects originating from electrode geometry, inter-electrode distance (IED), and conduction velocity, which must be considered for accurate signal interpretation.

Validation on hardware with stainless steel dry electrodes and custom analog front-end circuits confirmed simulation predictions. When compared to the industry-standard Quattrocento system using hydrogel electrodes, the modular sensor achieves comparable or superior SNR in generated input tests and human subject trials. The smaller electrode size and lower IED in the modular design provide improved spatial resolution and frequency representation, extending the detectable bandwidth beyond that of larger commercial electrodes, which induce low-pass filtering.

The investigation further highlights the important influence of electrode placement and electronic circuit architecture on critical EMG signal features such as amplitude, frequency content, and propagation delays of motor unit action potentials. In particular, single differential sensor modules demonstrated robust performance with high CMRR under balanced electrode-skin impedance, while double differential designs showed trade-offs in gain and noise performance.

User studies involving isometric biceps contractions across multiple subjects confirmed the system's capacity to detect physiologically relevant EMG signals with consistent quality. Notably, the battery-powered operation supports low susceptibility to powerline interference without reliance on notch filtering, underscoring its practical suitability for wearable neuromuscular interfaces.

In conclusion, this work delivers a versatile sEMG research platform that addresses the limitations of fixed commercial systems by enabling customizable electrode and circuitry configurations. This platform advances experimental EMG capabilities for

detailed physiological investigations and educational purposes.

Further investigations should address the total gain characteristics of the tested modules with the monopolar six-electrode (MP6EL) configuration, with focus on the frequency spectrum. It is expected that monopolar systems will exhibit lower mean frequencies compared to differential acquisition systems. Additionally, future work should compare the use of one of the six-electrode (6EL) electrodes as a reference in the monopolar setup against employing a distant reference electrode placed on a bony area. Such a comparison would provide insight into whether the additional complexity of a remote reference is justified or whether monopolar recordings can be reliably achieved within a single wristband module.

To comprehensively test transfer functions based on inter-electrode distance (IED), conduction velocity (CV), and electrode size, signals recorded with adhesive electrodes of varying sizes that provide excellent grounding should be evaluated. Reducing skin-electrode impedance remains an important factor; therefore, gold plating of stainless steel electrodes could be considered. This modification not only reduces skin-electrode impedance but also diminishes noise generated by chemical reactions between the skin or body fluids and the electrode material . Future work should also include systematic comparisons of electrodes with varying shapes, sizes, materials, and compliance characteristics, as well as benchmarking the current electrodes against high-density grids connected to the OT Bioelettronica Quattrocento system.

Bibliography

[1] MATS HAGBERG. "Work Load and Fatigue in Repetitive Arm Elevations." In: *Ergonomics* 24.7 (July 1981), pp. 543–555. ISSN: 0014-0139. DOI: 10.1080/00140138108924875. URL: https://doi.org/10.1080/00140138108924875 (visited on 02/03/2025).

[2] Paolo Visconti et al. "Technical Features and Functionalities of Myo Armband: An Overview on Related Literature and Advanced Applications of Myoelectric Armbands Mainly Focused on Arm Prostheses." In: *International Journal on Smart Sensing and Intelligent Systems* 11 (June 2018), pp. 1–25. DOI: 10.21307/ijssis-2018-005.

[3] IMGBIN.com. *Myo Armband Amazon.Com Bracelet Wristband PNG - Free Download*. URL: https://imgbin.com/png/xr4MH5at/myo-armband-amazon-com-bracelet-wristband-png (visited on 02/03/2025).

[4] Ruihao Zhang et al. "High-Performance Surface Electromyography Armband Design for Gesture Recognition." In: *Sensors* 23.10 (Jan. 2023), p. 4940. ISSN: 1424-8220. DOI: 10.3390/s23104940. URL: https://www.mdpi.com/1424-8220/23/10/4940 (visited on 02/03/2025).

[5] Elisa Romero Avila, Elmar Junker, and Catherine Disselhorst-Klug. "Introduction of a sEMG Sensor System for Autonomous Use by Inexperienced Users." In: *Sensors* 20.24 (Jan. 2020), p. 7348. ISSN: 1424-8220. DOI: 10.3390/s20247348. URL: https://www.mdpi.com/1424-8220/20/24/7348 (visited on 02/03/2025).

[6] *Human-Computer Input via an sEMG Wristband | Meta Quest-Blog*. URL: https://www.meta.com/blog/quest/surface-emg-wrist-white-paper-reality-labs (visited on 02/07/2025).

[7] Konrad Fruend. "Design of a Low-Cost Sensor Matrix for Use in Human-Machine Interactions on the Basis of Myographic Information." In: (Nov. 2019).

[8] Poul Rosenfalck. *Intra- and Extracellular Potential Fields of Active Nerve and Muscle Fibres.: A Physico-Mathematical Analysis of Different Models.* Copenhagen: Akademisk Forlag, (D.B.K), 1969.

[9] William C. Bowman. "Chapter 2 - Excitable Membranes." In: *Pharmacology of Neuromuscular Function (Second Edition)*. Ed. by William C. Bowman. Butterworth-Heinemann, Jan. 1990, pp. 8–35. ISBN: 978-0-7236-0913-1. DOI: 10.1016/B978-0-7236-0913-1.50006-2. URL: https://www.sciencedirect.com/science/article/pii/B9780723609131500062 (visited on 06/20/2025).

[10] J. Gordon Betts et al. *Anatomy and Physiology*. Open Textbook Library. Houston, Texas: OpenStax College, Rice University, 2017. ISBN: 978-1-947172-04-3.

[11] Edward George Tandy Liddell and Charles Scott Sherrington. "Recruitment and Some Other Features of Reflex Inhibition." In: *Proceedings of the Royal Society of London. Series B, Containing Papers of a Biological Character* 97.686 (Jan. 1997), pp. 488–518. DOI: 10.1098/rspb.1925.0016. URL: https://royalsocietypublishing.org/doi/10.1098/rspb.1925.0016 (visited on 06/18/2025).

[12] Dario Farina and Roberto Merletti. "Estimation of Average Muscle Fiber Conduction Velocity from Two-Dimensional Surface EMG Recordings." In: *Journal of Neuroscience Methods* 134.2 (Apr. 2004), pp. 199–208. ISSN: 0165-0270. DOI: 10.1016/j.jneumeth.2003.12.002.

[13] D. Farina and R. Merletti. "A Novel Approach for Estimating Muscle Fiber Conduction Velocity by Spatial and Temporal Filtering of Surface EMG Signals." In: *IEEE Transactions on Biomedical Engineering* 50.12 (Dec. 2003), pp. 1340–1351. ISSN: 1558-2531. DOI: 10.1109/TBME.2003.819847. URL: https://ieeexplore.ieee.org/abstract/document/1246373 (visited on 06/20/2025).

[14] *Surface Electromyography: Physiology, Engineering, and Applications | IEEE eBooks | IEEE Xplore*. URL: https://ieeexplore.ieee.org/book/7470984 (visited on 06/10/2025).

[15] C. J. De Luca et al. "Behaviour of Human Motor Units in Different Muscles during Linearly Varying Contractions." In: *The Journal of Physiology* 329 (Aug. 1982), pp. 113–128. ISSN: 0022-3751. DOI: 10.1113/jphysiol.1982.sp014293.

[16] C.J. Heckman and Roger M. Enoka. "Physiology of the Motor Neuron and the Motor Unit." In: *Clinical Neurophysiology of Motor Neuron Diseases*. Ed. by Andrew Eisen. Vol. 4. Handbook of Clinical Neurophysiology. Elsevier, 2004, pp. 119–147. DOI: 10.1016/S1567-4231(04)04006-7. URL: https://www.sciencedirect.com/science/article/pii/S1567423104040067.

[17] Elwood Henneman, George Somjen, and David O. Carpenter. "Functional Significance of Cell Size in Spinal Motoneurons." In: *Journal of Neurophysiology* 28.3 (May 1965), pp. 560–580. ISSN: 0022-3077. DOI: 10.1152/jn.1965.28.3.560. URL: https://journals.physiology.org/doi/abs/10.1152/jn.1965.28.3.560 (visited on 06/20/2025).

[18] E. J. Kupa et al. "Effects of Muscle Fiber Type and Size on EMG Median Frequency and Conduction Velocity." In: *Journal of Applied Physiology* 79.1 (July 1995), pp. 23–32. ISSN: 8750-7587. DOI: 10.1152/jappl.1995.79.1.23. URL: https://journals.physiology.org/doi/abs/10.1152/jappl.1995.79.1.23 (visited on 06/30/2025).

[19] Gary Kamen and David A. 1961 Gabriel. *Essentials of Electromyography*. Champaign u.a.: Human Kinetics, 2010. URL: http://bvbr.bib-bvb.de:8991/F?func=service&doc_library=BVB01&local_base=BVB01&doc_number=018958377&sequence=000004&line_number=0001&func_code=DB_RECORDS&service_type=MEDIA.

[20] Silvia Muceli and Roberto Merletti. "Tutorial. Frequency Analysis of the Surface EMG Signal: Best Practices." In: *Journal of Electromyography and Kinesiology* 79 (Dec. 2024), p. 102937. ISSN: 1050-6411. DOI: 10.1016/j.jelekin.2024.102937. URL: https://www.sciencedirect.com/science/article/pii/S1050641124000816 (visited on 07/25/2025).

[21] Carlo J De Luca. "SURFACE ELECTROMYOGRAPHY: DETECTION AND RECORDING." In: ().

[22] H.J. Landau. "Sampling, Data Transmission, and the Nyquist Rate." In: *Proceedings of the IEEE* 55.10 (Oct. 1967), pp. 1701–1706. ISSN: 1558-2256. DOI: 10.1109/PROC.1967.5962. URL: https://ieeexplore.ieee.org/abstract/document/1447892 (visited on 03/12/2025).

[23] John V. Basmajian. *Muscles Alive*. 1985. URL: http://archive.org/details/basmajian-muscles-alive (visited on 06/10/2025).

[24] *Electromyography: Physiology, Engineering, and Non-Invasive Applications | IEEE eBooks | IEEE Xplore*. URL: https://ieeexplore.ieee.org/book/5237323 (visited on 06/16/2025).

[25] R. Merletti and S. Muceli. "Tutorial. Surface EMG Detection in Space and Time: Best Practices." In: *Journal of Electromyography and Kinesiology* 49 (Dec. 2019), p. 102363. ISSN: 1050-6411. DOI: 10.1016/j.jelekin.2019.102363. URL: https://www.sciencedirect.com/science/article/pii/S1050641119302536 (visited on 06/24/2025).

[26] James C. Huhta and John G. Webster. "60-Hz Interference in Electrocardiography." In: *IEEE Transactions on Biomedical Engineering* BME-20.2 (Mar. 1973), pp. 91–101. ISSN: 1558-2531. DOI: 10.1109/TBME.1973.324169. URL: https://ieeexplore.ieee.org/document/4120603 (visited on 06/23/2025).

[27] R. Merletti and G. L. Cerone. "Tutorial. Surface EMG Detection, Conditioning and Pre-Processing: Best Practices." In: *Journal of Electromyography and Kinesiology* 54 (Oct. 2020), p. 102440. ISSN: 1050-6411. DOI: 10.1016/j.jelekin.2020.102440. URL: https://www.sciencedirect.com/science/article/pii/S1050641120300821 (visited on 06/20/2025).

[28] M.F. Chimene and R. Pallas-Areny. "A Comprehensive Model for Power Line Interference in Biopotential Measurements." In: *IEEE Transactions on Instrumentation and Measurement* 49.3 (June 2000), pp. 535–540. ISSN: 1557-9662. DOI: 10.1109/19.850390. URL: https://ieeexplore.ieee.org/document/850390 (visited on 06/23/2025).

[29] Karthik Soundarapandian and Mark Berarducci. "Analog Front-End Design for ECG Systems Using Delta-Sigma ADCs." In: (2009).

[30] Roberto Merletti et al. "Technology and Instrumentation for Detection and Conditioning of the Surface Electromyographic Signal: State of the Art." In: *Clinical biomechanics (Bristol, Avon)* 24 (Dec. 2008), pp. 122–34. DOI: 10.1016/j.clinbiomech.2008.08.006.

[31] J. C. Huhta and J. G. Webster. "60-HZ Interference in Electrocardiography." In: *IEEE transactions on bio-medical engineering* 20.2 (Mar. 1973), pp. 91–101. ISSN: 0018-9294. DOI: 10.1109/TBME.1973.324169.

[32] S. W. Johnson et al. "Miniature Skin-Mounted Preamplifier for Measurement of Surface Electromyographic Potentials." In: *Medical & Biological Engineering & Computing* 15.6 (Nov. 1977), pp. 710–711. ISSN: 0140-0118. DOI: 10.1007/BF02457936.

[33] R. Merletti et al. "Modeling of Surface Myoelectric Signals. I. Model Implementation." In: *IEEE Transactions on Biomedical Engineering* 46.7 (July 1999), pp. 810–820. ISSN: 1558-2531. DOI: 10.1109/10.771190. URL: https://ieeexplore.ieee.org/document/771190/ (visited on 08/11/2025).

[34] K. Roeleveld et al. "The Motor Unit Potential Distribution over the Skin Surface and Its Use in Estimating the Motor Unit Location." In: *Acta Physiologica Scandinavica* 161.4 (Dec. 1997), pp. 465–472. ISSN: 0001-6772. DOI: 10.1046/j.1365-201X.1997.00247.x.

[35] R. Merletti et al. "Modeling of Surface Myoelectric Signals. II. Model-based Signal Interpretation." In: *IEEE Transactions on Biomedical Engineering* 46.7 (July 1999), pp. 821–829. ISSN: 1558-2531. DOI: 10.1109/10.771191. URL: https://ieeexplore.ieee.org/document/771191/ (visited on 08/11/2025).

[36] D. A. Winter, A. J. Fuglevand, and S. E. Archer. "Crosstalk in Surface Electromyography: Theoretical and Practical Estimates." In: *Journal of Electromyography and Kinesiology: Official Journal of the International Society of Electrophysiological Kinesiology* 4.1 (1994), pp. 15–26. ISSN: 1050-6411. DOI: 10.1016/1050-6411(94)90023-X.

[37] Carina M. Germer et al. "Surface EMG Cross Talk Quantified at the Motor Unit Population Level for Muscles of the Hand, Thigh, and Calf." In: *Journal of Applied Physiology* 131.2 (Aug. 2021), pp. 808–820. ISSN: 8750-7587. DOI: 10.1152/japplphysiol.01041.2020. URL: https://journals.physiology.org/doi/full/10.1152/japplphysiol.01041.2020 (visited on 06/23/2025).

[38] Madeleine M. Lowery, Nikolay S. Stoykov, and Todd A. Kuiken. "A Simulation Study to Examine the Use of Cross-Correlation as an Estimate of Surface EMG Cross Talk." In: *Journal of Applied Physiology* 94.4 (Apr. 2003), pp. 1324–1334. ISSN: 8750-7587. DOI: 10.1152/japplphysiol.00698.2002. URL: https://journals.physiology.org/doi/full/10.1152/japplphysiol.00698.2002 (visited on 06/23/2025).

[39] Ken S. Frahm et al. "Surface EMG Crosstalk during Phasic Involuntary Muscle Activation in the Nociceptive Withdrawal Reflex." In: *Muscle & Nerve* 46.2 (2012), pp. 228–236. ISSN: 1097-4598. DOI: 10.1002/mus.23303. URL: https://onlinelibrary.wiley.com/doi/abs/10.1002/mus.23303 (visited on 03/06/2025).

[40] T. J. Koh and M. D. Grabiner. "Evaluation of Methods to Minimize Cross Talk in Surface Electromyography." In: *Journal of Biomechanics* 26 Suppl 1 (1993), pp. 151–157. ISSN: 0021-9290. DOI: 10.1016/0021-9290(93)90086-t.

[41] J. P. van Vugt and J. G. van Dijk. "A Convenient Method to Reduce Crosstalk in Surface EMG. Cobb Award-winning Article, 2001." In: *Clinical Neurophysiology: Official Journal of the International Federation of Clinical Neurophysiology* 112.4 (Apr. 2001), pp. 583–592. ISSN: 1388-2457. DOI: 10.1016/s1388-2457(01)00482-5.

[42] Luca Mesin. "Inverse Modelling to Reduce Crosstalk in High Density Surface Electromyogram." In: *Medical Engineering & Physics* 85 (Nov. 2020), pp. 55–62. ISSN: 1350-4533. DOI: 10.1016/j.medengphy.2020.09.011. URL: https://www.sciencedirect.com/science/article/pii/S1350453320301442 (visited on 06/23/2025).

[43] Julia W. Y. Kam et al. "Systematic Comparison between a Wireless EEG System with Dry Electrodes and a Wired EEG System with Wet Electrodes." In: *NeuroImage* 184 (Jan. 2019), pp. 119–129. ISSN: 1053-8119. DOI: 10.1016/j.neuroimage.2018.09.012. URL: https://www.sciencedirect.com/science/article/pii/S1053811918307961 (visited on 06/24/2025).

[44] B. Afsharipour, S. Soedirdjo, and R. Merletti. "Two-Dimensional Surface EMG: The Effects of Electrode Size, Interelectrode Distance and Image Truncation." In: *Biomedical Signal Processing and Control* 49 (Mar. 2019), pp. 298–307. ISSN: 1746-8094. DOI: 10.1016/j.bspc.2018.12.001. URL: https://www.sciencedirect.com/science/article/pii/S1746809418303008 (visited on 06/24/2025).

[45] Arnault H. Caillet et al. *Larger and Denser: An Optimal Design for Surface Grids of EMG Electrodes to Identify Greater and More Representative Samples of Motor Units*. Aug. 2023. DOI: 10.1101/2023.02.18.529050. URL: https://www.biorxiv.org/content/10.1101/2023.02.18.529050v3 (visited on 02/04/2025).

[46] R. Merletti and S. Muceli. "Tutorial. Surface EMG Detection in Space and Time: Best Practices." In: *Journal of Electromyography and Kinesiology* 49 (Dec. 2019), p. 102363. ISSN: 1050-6411. DOI: 10.1016/j.jelekin.2019.102363. URL: https://www.sciencedirect.com/science/article/pii/S1050641119302536 (visited on 06/16/2025).

[47] Isabella Campanini et al. "Fundamental Concepts of Bipolar and High-Density Surface EMG Understanding and Teaching for Clinical, Occupational, and Sport Applications: Origin, Detection, and Main Errors." In: *Sensors (Basel, Switzerland)* 22.11 (May 2022), p. 4150. ISSN: 1424-8220. DOI: 10.3390/s22114150. URL: https://www.ncbi.nlm.nih.gov/pmc/articles/PMC9185290/ (visited on 08/11/2025).

[48] B. Afsharipour, S. Soedirdjo, and R. Merletti. "Two-Dimensional Surface EMG: The Effects of Electrode Size, Interelectrode Distance and Image Truncation." In: *Biomedical Signal Processing and Control* 49 (Mar. 2019), pp. 298–307. ISSN: 1746-8094. DOI: 10.1016/j.bspc.2018.12.001. URL: https://www.sciencedirect.com/science/article/pii/S1746809418303008 (visited on 02/17/2025).

[49] *INA128 Data Sheet, Product Information and Support | TI.Com*. URL: https://www.ti.com/product/INA128 (visited on 08/11/2025).

[50] *Medical Instrumentation Application and Design*. Fifth edition. Hoboken, NJ: Wiley, 2020. ISBN: 978-1-119-45733-6. URL: http://swbplus.bsz-bw.de/bsz1685845673cov.htm (visited on 06/23/2025).

[51] *Inside Myo | Myo Armband Teardown | Adafruit Learning System*. URL: https://learn.adafruit.com/myo-armband-teardown/inside-myo (visited on 08/06/2025).

[52] Ulysse Côté-Allard et al. "A Low-Cost, Wireless, 3-D-Printed Custom Armband for sEMG Hand Gesture Recognition." In: *Sensors* 19.12 (Jan. 2019), p. 2811. ISSN: 1424-8220. DOI: 10.3390/s19122811. URL: https://www.mdpi.com/1424-8220/19/12/2811 (visited on 08/06/2025).

[53] Eisa Aghchehli et al. "Medium Density EMG Armband for Gesture Recognition." In: *Frontiers in Neurorobotics* 19 (Apr. 2025), p. 1531815. ISSN: 1662-5218. DOI: 10.3389/fnbot.2025.1531815. URL: https://www.ncbi.nlm.nih.gov/pmc/articles/PMC12075175/ (visited on 08/30/2025).

[54] CTRL-labs at Reality Labs et al. *A Generic Noninvasive Neuromotor Interface for Human-Computer Interaction*. July 2024. DOI: 10.1101/2024.02.23.581779. URL: https://www.biorxiv.org/content/10.1101/2024.02.23.581779v2 (visited on 02/05/2025).

[55] Abhimanyu Ghoshal. *Meta Wants to Replace Your Mouse and Keyboard with This Bracelet*. July 2025. URL: https://newatlas.com/wearables/meta-mouse-keyboard-bracelet-semg-rd/ (visited on 08/07/2025).

[56] Dario Farina and Roberto Merletti, eds. *Surface Electromyography: Physiology, Engineering, and Applications*. IEEE Press Series on Biomedical Engineering. Piscataway, NJ: IEEE Press, 2016. ISBN: 978-1-118-98702-5 978-1-119-08290-3 978-1-119-08293-4. DOI: 10.1002/9781119082934.

[57] *Wearable Device for Restoring Movement Aims to Deliver Hope to Stroke Patients | Imperial News | Imperial College London*. Aug. 2025. URL: https://www.imperial.ac.uk/news/267033/wearable-device-restoring-movement-aims-deliver/ (visited on 08/08/2025).

[58] Neubond. *Neubond: Revolutionising Neuro-Rehabilitation*. URL: https://neubond.co.uk/ (visited on 08/08/2025).

[59] Neubond. *Neubond: Science Behind the Device*. URL: https://neubond.co.uk/science (visited on 08/08/2025).

[60] Janne M. Hahne et al. "A Novel Percutaneous Electrode Implant for Improving Robustness in Advanced Myoelectric Control." In: *Frontiers in Neuroscience* 10 (Mar. 2016), p. 114. ISSN: 1662-4548. DOI: 10.3389/fnins.2016.00114. URL: https://www.ncbi.nlm.nih.gov/pmc/articles/PMC4814550/ (visited on 08/09/2025).

[61] Davide Brunelli et al. "Low-Cost Wearable Multichannel Surface EMG Acquisition for Prosthetic Hand Control." In: *2015 6th International Workshop on Advances in Sensors and Interfaces (IWASI)*. June 2015, pp. 94–99. DOI: 10.1109/IWASI.2015.7184964. URL: https://ieeexplore.ieee.org/document/7184964 (visited on 08/09/2025).

[62] *Stable Myoelectric Control of a Hand Prosthesis Using Non-Linear Incremental Learning*. URL: https://www.researchgate.net/publication/260684466_Stable_Myoelectric_Control_of_a_Hand_Prosthesis_using_Non-Linear_Incremental_Learning (visited on 08/31/2025).

[63] *Elektrode | Sensibles Herzstück*. URL: https://www.ottobock.com/de-de/product/13E200-61664 (visited on 08/09/2025).

[64] *Quattrocento*. URL: https://otbioelettronica.it/en/quattrocento/ (visited on 08/09/2025).

[65] Agnese Grison et al. "Unlocking the Full Potential of High-density Surface EMG: Novel Non-invasive High-yield Motor Unit Decomposition." In: *The Journal of Physiology* 603.8 (Apr. 2025), pp. 2281–2300. ISSN: 0022-3751. DOI: 10.1113/JP287913. URL: https://www.ncbi.nlm.nih.gov/pmc/articles/PMC12013791/ (visited on 08/09/2025).

[66] Raul C. Sîmpetru et al. "MyoGestic: EMG Interfacing Framework for Decoding Multiple Spared Motor Dimensions in Individuals with Neural Lesions." In: *Science Advances* 11.15 (), eads9150. ISSN: 2375-2548. DOI: 10.1126/sciadv.ads9150. URL: https://www.ncbi.nlm.nih.gov/pmc/articles/PMC11980827/ (visited on 08/09/2025).

[67] Luis Pelaez Murciego et al. "Reducing the Number of EMG Electrodes during Online Hand Gesture Classification with Changing Wrist Positions." In: *Journal of NeuroEngineering and Rehabilitation* 19.1 (July 2022), p. 78. ISSN: 1743-0003. DOI: 10.1186/s12984-022-01056-w. URL: https://doi.org/10.1186/s12984-022-01056-w (visited on 08/09/2025).

[68] A Del Vecchio and D Farina. "Interfacing the Neural Output of the Spinal Cord: Robust and Reliable Longitudinal Identification of Motor Neurons in Humans." In: *Journal of Neural Engineering* 17.1 (Dec. 2019), p. 016003. ISSN: 1741-2552. DOI: 10.1088/1741-2552/ab4d05. URL: https://dx.doi.org/10.1088/1741-2552/ab4d05 (visited on 08/12/2025).

[69] Brendan B. Murphy et al. "Time Evolution of the Skin–Electrode Interface Impedance under Different Skin Treatments." In: *Sensors* 21.15 (Jan. 2021), p. 5210. ISSN: 1424-8220. DOI: 10.3390/s21155210. URL: https://www.mdpi.com/1424-8220/21/15/5210 (visited on 03/10/2025).

[70] Zinvi Fu et al. "Optimizing Surface Electromyography Acquisition without Right Leg Drive Circuit." In: *International Journal of Engineering Science Technologies* 1 (Jan. 2017). DOI: 10.29121/IJOEST.v1.i1.2017.02.

[71] Aura Polo Llanos, Pedro Narváez, and Carlos Robles. "Implementation of a Cost-Effective Didactic Prototype for the Acquisition of Biomedical Signals." In: *Electronics* 7 (May 2018), p. 77. DOI: 10.3390/electronics7050077.

[72] Aura Polo, Pedro Narvaez, and Carlos Robles Algarín. "Implementation of a Cost-Effective Didactic Prototype for the Acquisition of Biomedical Signals." In: *Electronics* 7.5 (May 2018), p. 77. ISSN: 2079-9292. DOI: 10.3390/electronics7050077. URL: https://www.mdpi.com/2079-9292/7/5/77 (visited on 08/12/2025).

[73] D. Farina et al. "Assessment of Average Muscle Fiber Conduction Velocity From Surface EMG Signals During Fatiguing Dynamic Contractions." In: *IEEE Transactions on Biomedical Engineering* 51.8 (Aug. 2004), pp. 1383–1393. ISSN: 0018-9294. DOI: 10.1109/TBME.2004.827556. URL: http://ieeexplore.ieee.org/document/1315860/ (visited on 02/21/2025).

[74] Tadashi Masuda, Hisao Miyano, and Tsugutake Sadoyama. "The Position of Innervation Zones in the Biceps Brachii Investigated by Surface Electromyography." In: *IEEE Transactions on Biomedical Engineering* BME-32.1 (Jan. 1985), pp. 36–42. ISSN: 1558-2531. DOI: 10.1109/TBME.1985.325614. URL: https://ieeexplore.ieee.org/document/4121922/ (visited on 08/23/2025).

[75] *AD623 | Datasheet and Product Info Single Supply, Rail-Rail, Low Cost Instrumentation Amplifier | Analog Devices*. URL: https://www.analog.com/en/products/ad623.html (visited on 08/20/2025).

[76] *AD8422 | Datasheet and Product Info High Performance, Low Power, Rail-to-Rail Precision Instrumentation Amplifier | Analog Devices*. URL: https://www.analog.com/en/products/ad8422.html (visited on 08/20/2025).

[77] *INA333 Data Sheet, Product Information and Support | TI.Com*. URL: https://www.ti.com/product/INA333 (visited on 08/20/2025).

[78] *AD8224 | Datasheet and Product Info Precision, Dual-Channel, JFET Input, Rail-to-Rail Instrumentation Amplifier | Analog Devices*. URL: https://www.analog.com/en/products/ad8224.html (visited on 08/20/2025).

[79] *LTC6373 Datasheet and Product Info | Analog Devices*. URL: https://www.analog.com/en/products/ltc6373.html (visited on 08/20/2025).

[80] *AD8220 | Datasheet and Product Info JFET Input Instrumentation Amplifier with Rail-to-Rail Output | Analog Devices*. URL: https://www.analog.com/en/products/ad8220.html (visited on 08/20/2025).

[81] *AD8235 | Datasheet and Product Info 40 µA Micropower Instrumentation Amplifier in WLCSP Package | Analog Devices*. URL: https://www.analog.com/en/products/ad8235.html (visited on 08/20/2025).

[82] *AD8244 | Datasheet and Product Info Single-Supply, Low Power, Precision FET Input Quad Buffer | Analog Devices*. URL: https://www.analog.com/en/products/ad8244.html (visited on 08/20/2025).

[83] *TPS60402 Data Sheet, Product Information and Support | TI.Com*. URL: https://www.ti.com/product/TPS60402 (visited on 08/20/2025).

[84] Guangli Li, Sizhe Wang, and Yanwen Y. Duan. "Towards Conductive-Gel-Free Electrodes: Understanding the Wet Electrode, Semi-Dry Electrode and Dry Electrode-Skin Interface Impedance Using Electrochemical Impedance Spectroscopy Fitting." In: *Sensors and Actuators B: Chemical* 277 (Dec. 2018), pp. 250–260. ISSN: 0925-4005. DOI: 10.1016/j.snb.2018.08.155. URL: https://www.sciencedirect.com/science/article/pii/S0925400518315934 (visited on 08/22/2025).

[85] E. Huigen, A. Peper, and C. A. Grimbergen. "Investigation into the Origin of the Noise of Surface Electrodes." In: *Medical & Biological Engineering & Computing* 40.3 (May 2002), pp. 332–338. ISSN: 0140-0118, 1741-0444. DOI: 10.1007/BF02344216. URL: http://link.springer.com/10.1007/BF02344216 (visited on 02/21/2025).

[86] Ana Arché-Núñez et al. "Bio-potential noise of dry printed electrodes: physiology versus the skin-electrode impedance." In: *Physiological Measurement* 44.9 (2023), p. 095006. ISSN: 0967-3334, 1361-6579. DOI: 10.1088/1361-6579/acf2e7. URL: https://publikationen.bibliothek.kit.edu/1000163140 (visited on 05/28/2025).

Abbreviations

HMI Human-Machine interfaces

sEMG Surface Electromyography

DLR German Aerospace Senter

MU motor unit

MUAP motor unit action potential

CV conduction velocity

FFT fast fourier transformation

SNR signal-to-noise ratio

IED inter-electrode distance

PLI Powerline interference

CMRR common-mode rejection ratio

SD Single differential

DD Double differential

MP Monopolar

RMS root mean square

HD-sEMG high-density surface electromyography

DRL driven right leg

ECG electrocardiography

ADC analog-to-digital converter

IMU inertial measurement unit

RD research device

EEG electroencephalography

DAQ Data acquisition

PCB printed circuit board

IA instrumentation amplifier

op-amp operational amplifier

LSB least significant bit

PDS power density spectrum

SPI serial peripheral interface

COM communication

VRMS root mean square voltage

List of Figures

List of Tables